Plasmonic synergism in tailored metal–carbon interfaces for real-time single molecular level sniffing of PFOS and PFOA

Dipin Thacharakkal [a], Seemesh Bhaskar [a,b], Tanu Sharma [a], Gopalan Rajaraman [a,*], Sai Sathish Ramamurthy [b,*], Chandramouli Subramaniam [a,*]

[a] Department of Chemistry, Indian Institute of Technology, Bombay, Powai, Mumbai, Maharashtra 400076, India
[b] Department of Chemistry, Sri Sathya sai Institute of Higer Learning, Anantapur, AndhraPradesh, 515134, India

ARTICLE INFO

ABSTRACT

Generating plasmonic hot-spots through engineering of nanoscale interfaces offers exciting opportunities towards point-of-care analytical detection. The mutual trade-off between ultra-high sensitivity, specificity and reliability are major drawbacks for practical applicability with real-time samples. Fundamentally these originate from low photonic mode density, high ohmic losses, temporally fluctuating and chemically indistinguishable nature of electromagnetic hot-spots. This work describes synergism of metallic plasmons from tailored interfaces of Ag-Au nanoalloys with conical nanocavities of nanocarbon florets (NCF), leading to strong metal-dielectric interfacial coupling. Such, Ag-Au-NCF nanohybrid delivers an unprecedented 1517-fold enhancement in surface-plasmon coupled directed emission (SPCE) of Rhodamine B (RhB) leading to robust (relative standard deviation, RSD < 10 %) single-molecular-level detection of spectroscopically-silent perfluoroalkyl substances (PFAS). The limit-of-detection demonstrated (PFOS = 0.005 ppt) is one-thousand times better than WHO recommendation and surpasses all existing reports. The specific cation–anion interactions between RhB and PFAS are substantiated through density functional calculations that concur with experimental findings. Finally, the emission from this SPCE platform can be visually tracked through a smartphone camera over wide range of PFOS concentrations (0.005–5000000 ppt) in water samples (lake, river, tap, drinking and ocean) and blood-plasma, offering transformative opportunities in analytical sciences.

1. Introduction

Fluorine-containing poly- and perfluoroalkyl substances (PFAS) constitute a major class of emerging contaminants in water, whose ubiquitous occurrence extends to water bodies, soil, aquatic life, vegetation and humans. This category of compounds have been classified as 'forever chemicals' on account of their long persistence and chemical stability that adversely effects the immunal, developmental, metabolic, and endocrinal systems of all life forms [1]. The accumulative nature of such chemicals implies that consistent exposure at insignificant concentrations is sufficient to cause health complications ranging from chronic prostate and kidney cancer, anemia, pancreatic diseases, coronary artery disease, hypertension, and thyroid dysfunction to fetal development effects [2–5]. The magnitude and severity of the PFAS is evident from estimates of ~54–83 % of the US population suffering from the exposure and contamination of PFAS in drinking water, with several countries banning its usage [6]. The acceptable limit for PFAS in

drinking water is stipulated by WHO to be 70 ng/L (70 ppt) for lifetime exposure [7]. The current gold standard for the detection of PFAS is high-performance liquid chromatography (HPLC) and gas chromatography (GC) coupled with mass spectrometry (MS), providing a detection limit of ~0.5 ppt [8]. However, the cumbersome instrumentation requiring sophisticated, time-intensive methodologies, complex sample preparation requirements, exhaustive sample processing and limitations in nature of samples have severely restricted its applicability, particularly for on-field applications. Such complexity and inaccessibility of testing originating from the spectroscopically silent nature of PFAS, leads to severe damages to environment and ecosystem [9].

Accordingly, the two main approaches for the detection of PFAS have focused on electrochemical and optical methodologies. While electrochemical techniques are favored for their efficient signal transaction pathways, the lack of clear electrochemical redox behavior, poor solubility, hydrophobic nature, and low reactivity of PFAS have proven to be significant disadvantages that limit the sensitivity and reliability of

detection [10]. In this direction, electrochemical impedance spectroscopy provides a viable alternative and has been demonstrated to achieve a LOD of 0.5 ppt by Cheng et al [11]. However, such approaches suffer from low specificity and reliability of detection in real-time, on-field testing. On the other hand, optical detection approaches such as fluorimetry, [12] photoluminescence, [13] electroluminescence, [14] colorimetry [15], and surface-enhanced Raman scattering [16] have exploited sensitive light-matter interactions to demonstrate the specificity of detection, at the cost of sensitivity. For instance, fluorimetry fails below a threshold concentration of ~10^{-11} M (5 ppt) in case of PFAS [17–19]. The spectroscopically silent nature of PFAS has proved to be a major obstacle in achieving the synergistic combination of ultra-sensitive, specific, and reliable detection. In addition, the cumbersome instrumentation involved in optical techniques along with the requirement of separate transducer have been severe limitations for sensible detection and real-time environmental monitoring of PFAS. Our current inability to reliably detect PFAS with ultra-high sensitivity is evident from Fig. S1 that summarizes the state-of-the-art detection techniques reported (Fig. S1). Thus, a sensing platform that combines the specificity of optical techniques with the sensitivity and reliability of electrochemical platforms to provide a direct visual readout is an immediate and important requirement.

Recent years have witnessed greater utilization of light-matter interactions at nanoscale dimensions for enhancing the spectroscopic signals through surface enhanced-Raman scattering (SERS) and surface plasmon coupled emission (SPCE) platforms [20–23]. Radiating dipoles of the analyte localized within the electromagnetic hot-spots of plasmonic assemblies experiences synergistic coupling leading to high excitation and emission rates [24–29]. The pioneering works of Lakowicz and co-workers explored such architectures on metallic thin films sustaining propagating surface plasmon polaritons (SPPs) [30,31,32]. Study of Ag nanoparticles (Ag NPs) over metallic thin films yielded 60-fold higher intensity of emission over those obtained through conventional spectrophotometer [32]. Following this revelation, our laboratory investigated the prominence of inter-plasmonic photonic coupling with the use of myriad nanosystems, including intermetallics, [33] low-dimensional carbon substrates [34,35], and coinage metal-dielectric hybrids [36,37] in addition to exploring their synergistic nano-assemblies. These systems provided new horizons in understanding the contribution from delocalized Bragg plasmons and localized Mie plasmons as well the cavity and void effects at fundamental level, to broaden the scope of nanoplasmonics-based detection systems [38–40]. In spite of these fundamental and applicative developments, the main challenges that confront SPCE-based detection systems remain their (i) poor fluorescence enhancements [41,42], (ii) radiative damping [43,44], (iii) low-quality factor [45], (iv) Ohmic losses with the use of Au and Ag NPs [46–48], all of which directly contributes to low sensitivity of detection [49]. Overcoming these fundamental limitations would provide a viable path towards the development of portable sensors that combines ultra-high, single molecular level sensitivity with reliability of sensing and thereby achieve first-line defenders for robust and early-stage identification of PFAS.

In this direction, we establish design principles to synergistically combine a non-plasmonic, multi-scale porous nanostructured hard-carbon floret (NCF) with plasmonic metal nanostructures that overcome the fundamental limitations described above. Specifically, the convergence of inter-plasmonic, intra-plasmonic, and dielectric-mediated void plasmons in Ag-Au-NCF curtails the ohmic-losses and produces highly confined electromagnetic hot-spots at the metal-NCF interface. Consequently, we achieve an unprecedented 1517-fold directed enhancement of fluorescence emission. We leverage this powerful concept to demonstrate direct visual detection of PFOS (Heptadecafluorooctanesulfonic acid) and PFOA (Perfluorooctanoic acid) at 10 aM (5×10^{-3} ppt) and 1fM (4.14×10^{-1} ppt) levels, respectively. While this forms the state-of-art in terms of the detection limit for the emerging class of contaminants (PFAS), the SPCE platform also exhibits ultra-high sensitivity (PFOS = 155.78 counts, PFOA = 144.98 counts) and linearity of signals over a large range of concentrations spanning 8–10 orders of magnitude. Importantly, the specificity of detection is demonstrated in range of samples such as tap water, river water (Chitravathi, Andrapradesh, India), drinking water, lake water (Powai Lake, Maharashtra, India) and ocean water (Juhu Chowpatty Beach, Maharashtra, India) and blood-plasma. Such combination of high detection metrics originates from charge-transfer-based interaction between the fluorophore (RhB) and analyte (PFOA/PFOS). We firmly believe that the low-cost, portable smartphone-based detection system developed herewith would be realistically integrated with the rapidly growing artificial intelligence tools such as neural networks to generate and asses the environmental water and health conditions at remote locations, with an ease to record, transmit, compare and analyze the data from different parts of the geolocations, thereby enabling environmental surveillance, water quality managers, and health policymakers to make appropriate decisions in real-time basis.

2. Materials and methods

2.1. Chemicals and materials

50 nm Ag thin film coated on Pyrex slide (1 mm) with 5 nm silica layer on it, was purchased from EMF Corp, USA. All the chemicals used are of analytical grade and are used as received without any further purification. $HAuCl_4$, $AgNO_3$, Cetyltrimethylammonium bromide (CTAB), Tetraethyl orthosilicate (TEOS), urea, Rhodamine B (RhB), Polyvinyl alcohol (PVA) [molecular weight 85,000–12, 4000 g/mol; degree of hydrolysis 86–89 %] and phosphate-buffered saline tablets (PBS, P4417) were procured from Sigma-Aldrich. Cyclohexane, pentanol, perfluorooctanoic acid (PFOA), Heptadecafluorooctanesulfonic acid (PFOS), $CaCl_2$, $CdCl_2$, CH_3COONa, glucose, $MgCl_2$, $ZnCl_2$, KCl, NaCl, $NaNO_3$, thiourea, Na_2SO_4 and NaOH were procured from Merck. Water samples from different resources are used in this study. Such as, tap water, river water (Chitravathi, Andrapradesh, India), drinking water, lake water (Powai Lake, Maharashtra, India) and ocean water (Juhu Chowpatty Beach, Maharashtra, India). The spiking studies using blood-plasma are collected from healthy patient (control subjects of the DST-Technology Development Programme, project code: IDP/MED/19/2016) as part of the biomedical research (at STAR laboratory, SSSIHL). All reagents used in this study were of analytical grade. All the glassware used for synthesis were cleaned with aqua regia. Following this, they are rinsed with Milli-Q water and with distilled ethanol. Further, they were well-dried before use.

2.2. Instrumentation and characterization

The synthesized NCF and metal decorated NCF were characterized using various techniques. The structural properties, morphology and size distribution of metal nanoparticles were obtained by transmission electron microscopy (TEM) using Thermo Scientific, Themis 300 G3. TEM samples were prepared by drop casting dilute solution of Ag-Au-NCF-10 on carbon coated copper grid followed by drying in ambient atmosphere. Powder X-ray diffraction (XRD) traces were collected on Rigaku Smartlab SE diffractometer using Cu-Kα radiation 1.514 Å and all the samples were scanned in the 2θ range of 5–80° at a step scan of 5° per minute. X-ray photoelectron spectroscopy (XPS) analysis were performed using Kratos Analytical, AXIS Supra, Shimadzu group. The solid-state UV–Visible absorption spectrum were used to analyse the sample (Jasco 770- UV–VIS-NIR). The fluorescence spectra were obtained via Horiba Fluoromax 4 Spectrofluorometer. Zeta potential of RhB and RhB-PFOS mixture was measured using Anton Parr (model of Litesizer 500) by using Omega cuvette.

2.3. SPCE experimentation

All the SPCE experiments were performed in reverse Kretchmann (RK) configuration by mounting the prism on a calibrated 360° rotating stage (Fig. S2) [29,30]. The main component of the SPCE substrate is a Pyrex slide coated with a 50 nm thin film of Ag. The Ag coated Pyrex slide is attached to the hemicylindrical BK7 prism by using index matching fluid glycerol (1.47) and it is mounted on a rotating stage. A continuous wave laser source operating at a wavelength of 532 nm (with a laser power 5 mW) illuminates the SPCE substrate and the surface plasmon-coupled emission was collected from distal part of the prism. A 550 nm long wave pass filter and a polarizer are used to collect the coupled emission from the distal part of the prism. The polarizer is placed in the horizontal and vertical orientation to confirm the p-polarized SPCE characteristics. A P600-2-VIS-NIR fiber (Wavelength Range: 400 nm − 2.1 μm, Fiber Core Size: 600 μm, Length: 2 m, Jacket: PVDF zip tube) is utilized for efficient signal collection. To reduce the cost of detector systems, we replaced the costly spectrophotometer with a smartphone-based detector, as illustrated in Fig. S2. The plasmonic interfaces: spacer, cavity, and ext. cavity employed in SPCE experimentation is elaborated in subsequent sections. The emission is captured using a smartphone camera, and the resulting images are analyzed using the Color Grab app, which can be downloaded from the Google Play Store. The SPCE measurements were carried out under reverse Kretchmann geometry to estimate the SPCE enhancements as [50].

$$SPCE\ enhancement = \frac{SPCE\ intensity\ under\ given\ conditions\ (counts)}{Free - space\ intensity\ under\ identical\ conditions\ (counts)}$$

The SPCE thin films were characterized through both electron microscopy and absorbance spectroscopy. For the scanning electron microscopy (SEM), effective concentrations of polyvinyl alcohol (400 μl of 2 wt%) was mixed with RhB (200 μl of 1 mM) and Ag-Au-NCF-10 (200 μl of 0.04 wt%) in aqueous medium (distilled water, pH 7.0). The resulting dispersion was spin-coated at 3000 rpm on silicon/quartz substrates and air-dried to yield, continuous and uniform films. These were subsequently characterized by optical microscope (Olympus microscope of DSX series) and SEM (Dual vacuum HR SEM, JEOL). The thickness of the films were estimated using optical absorption as

$$Thickness = \frac{2.303A}{\alpha}$$

where A and α represents the absorbance and extinction coefficient of the PVA thin films. This information, the corresponding images and the spectra are provided in the supporting information.

2.3.1. Preparation of SPCE substrate

We have utilized three different nanointerfaces (Fig. 2a), namely (a) Spacer configuration, (b) Cavity configuration and (c) Extended cavity (ext. cavity). The preparation of each nanointerface is explained below

(a) Spacer configuration: The SPCE substrate (Pyrex slide coated with a 50 nm thin film of Ag) was spin coated with 0.02 wt% of Metal-NCF hybrid in 2 wt% of poly-vinyl alcohol (PVA) followed by the further incorporation of 1 mM RhB in PVA on the same substrate. Thus, the interaction between the Metal-NCF hybrid with the RhB is mediated by the PVA.

(b) Cavity configuration: The SPCE substrate was spin coated with premixed PVA, Metal-NCF and RhB having the same concentration of spacer configuration providing direct interaction between the radiating dipole of RhB with the metal-NCF hybrid.

(c) Ext. cavity: RhB is sandwiched between the metal-NCF hybrid and PVA. The SPCE substrate was spin coated with 1 mM RhB in 2 wt% of poly-vinyl alcohol (PVA) followed by the further coating of Metal-NCF hybrid in PVA on the same substrate.

3. Preparation for SPCE substrate for PFAS sensing

1517-fold enhancement in SPCE of RhB in cavity configuration with Ag-Au-NCF-10 nanohybrid is utilised for the sensing of PFOS and PFOA. Here, RhB is mixed with arbitrary concentration of PFAS followed by the addition of Ag-Au-NCF-10 and 2 wt% PVA and the premixed mixture was spin coated over SPCE substrate to record the emission intensity.

3.1. Computational methods

The Gaussian 16 [51] suite was utilized for optimization and AIM analysis [52,53], with the B3LYP functional [54,55] and the 6-31G * basis [56] set being employed. Additionally, the empirical dispersion D3 [57] was incorporated to consider non-covalent interactions. The absorption spectrum of RhB-PFOS and RhB-PFOA was analyzed using programs from the ORCA suite [58]. The TD-DFT approach was employed in these calculations, and the BP86 functional [59] and the TZVP basis set were used for all atoms. Furthermore, the conductor-like polarizable continuum model (CPCM) solvation model [60] was incorporated to account for solvation effects arising from water.

3.2. Synthesis of dendritic fibrous nanosilica (DFNS)

At room temperature, cetyltrimethylammonium bromide (CTAB) (2 g, 0.005 mol) and urea (2.4 g, 0.04 mol) were mixed in 100 mL of water. To this solution, TEOS (4.7 g, 0.02 mol) in 100 mL of cyclohexane is added in dropwise and mixed for 1 h followed by the addition of 1-pentanol (7.57 g, 0.086 mol). The mixture was refluxed at 82 °C using an oil bath and kept for 12 h under ambient stirring. The obtained product was washed with water and ethanol, and dried at 80 °C. Finally, the white powder was calcined at 550 °C for 6 h to remove the reactants to get dendritic fibrous nanosilica [50].

3.3. Synthesis of nanocarbon floret (NCF)

NCF was prepared by a hard template method using DFNS as the template and acetylene as carbon source. The prepared DFNS was heated in a quartz tube at 740 °C under a helium atmosphere (700 sccm). Acetylene gas was passed through the tube for a duration of 10 min. The resulting black powder was stirred with 1 M NaOH to remove the DFNS followed by washing with water until the pH of the filtrate became neutral. The resulting black powder was dried in oven at 80 °C to obtain nanocarbon florets [50].

3.4. Synthesis of metal-dielectric nanohybrid

Schematic for the synthesis of Ag, Au and Ag-Au decorated over NCF is shown in the Fig. 1a. 1 mM aqueous solution of $AgNO_3$ / $HAuCl_4$ is stirred with 0.1 % of NCF (w/v) under sunlight for different time intervals 1, 5, 10 and 20 min. The obtained product is immediately centrifuged and dried in hot air oven at 70 °C. Similarly, the Ag-Au hybrid was decorated as same protocol by mixing $AgNO_3$ and $HAuCl_4$ with 0.1 % of NCF. The obtained product was labelled according to their time of solar irradiation.
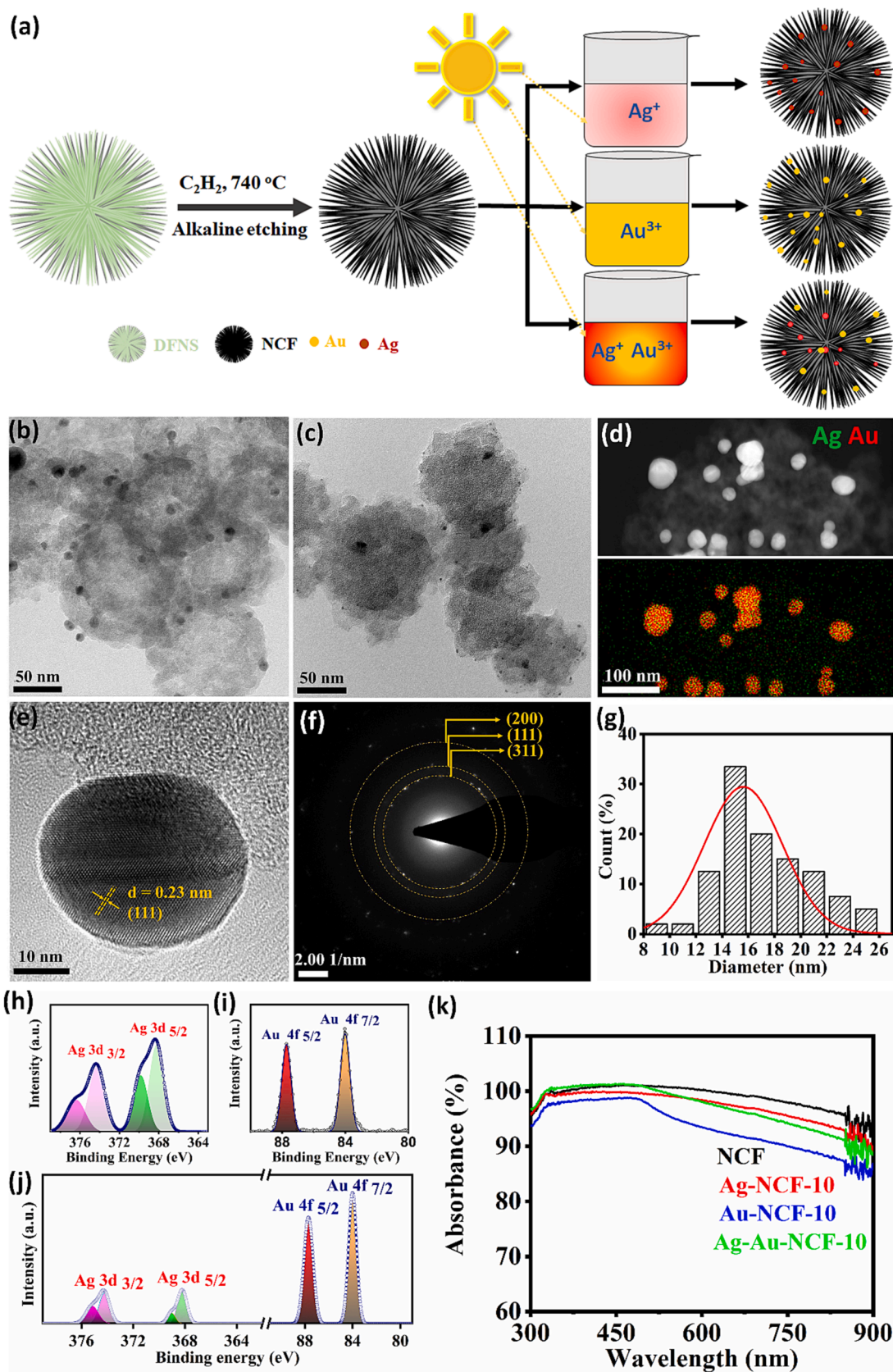
Fig. 1. (a) Schematic representation of fabrication of NCF followed by photothermal one-pot synthesis of Ag-NCF, Au-NCF and Ag-Au-NCF. (b,c,e) TEM images, (d) HAADF imaging and (f) SAED of Ag-Au-NCF-10. (g) Histogram showing the size distribution of metallic nanoalloy (Ag-Au) on NCF obtained after 10 min of solar irradiation. High resolution XPS of (h) Ag-NCF-10, (i) Au-NCF-10 and (j) Ag-Au-NCF-10, (k) absorption spectra of NCF, Ag-NCF-10, Au-NCF-10 and Ag-Au-NCF-10.

4. Result and discussion

Universally, the reliability and sensitivity of SPCE platforms are dictated by the accessible photonic mode density (PMD) at nanoscale interfaces and efficient suppressing of non-radiative phenomena. Nanostructured metal-based SPCE platforms, such as those of Ag, Au, Pt, and Pd, exhibits significant ohmic losses besides suffering from unavoidable surface oxidation. Similarly, spectral broadening is also observed in SPR resonance while employing metal thin films in combination with metal nanoparticles. All these phenomena contribute to lowering of PMD [61–65]. In addition, the exponential decrease in electromagnetic field enhancements poses significant challenges in confining the analyte within a microscopic zone of activity resulting in inevitable quenching phenomena and causing large variability in the results.

4.1. Fabrication and characterization of metal-nanocarbon interfaces for SPCE platforms

In order to overcome these shortcomings, our approach focused on porosity engineering of hard-carbon frameworks whose morphology would serve as dielectric-based optical microscale cavities. Furthermore, the large and easily accessible surface area of such nanostructures would serve as anchoring surfaces for plasmonic materials with higher PMD and lower ohmic losses. In this direction, templating of dendritic fibrous nanosilica (DFNS) by gas phase carbon deposition yielded unique, open-ended, nanostructured hard-carbon florets (NCF) that exhibit multi-dimensional porosity and large accessible surface area ($743 \ m^2 g^{-1}$) [66]. Importantly, three-dimensional spherical assemblies of graphitic lamellae mimic optical microcavities for effective broadband absorption [67]. The large surface area and graded pore structures of NCF also provides conducive surface for anchoring of plasmonic materials. Such hybrid dielectric-plasmonic assemblies are therefore expected to achieve the synergistic combination of electromagnetic plasmonic hot-spots and π-π^* dielectric driven SPCE enhancements leading to ultra-high sensitivity with chemically tailored specificity. NCF exhibits the combination of hard-carbon framework and conically graded morphology, both of which act synergistically to achieve highly efficient light entrapment and absorption [66–71]. While this is beneficial for the targeted SPCE platform, we extend our design principles to construct higher ordered nanoarchitectures that leverages the advantages of both dielectric and plasmonic platforms. Accordingly, a single-step photo-driven anchoring and growth of nano-dimensional Au, Ag, and Ag-Au alloy within the cavities of NCF was achieved (Fig. 1a). This was further assisted by the intrinsic functional groups (–OH, –COOH) created on the terminal graphitic domains during the fabrication of NCF (Fig. S3). It is important to note that photo exposure of the corresponding metal ions either led to their uncontrolled reduction (in case of Ag^+), resulting in bulk silver films or afforded no reaction (in case of Au^{3+}). Therefore, the strong photothermal ability of NCF is a primary factor driving the reduction of metal ion precursors. Further, the presence of suitable anchoring points on the surface of NCF and its confined conical geometry are deterministic factors that control the dimensions of resulting metallic nanostructures. Accordingly, the kinetics of nucleation and growth of metallic nanostructures (Au, Ag, and Ag-Au) were controlled by varying the time of solar irradiation ($2000 \ Wm^{-2}$). The samples thus obtained were labelled as Au-NCF-x, Ag-NCF-x, and Ag-Au-NCF-x, where × denotes the time of solar irradiation (x = 1, 5, 10, and 20 min), with metal-NCF hybrids used to denote them collectively. The formation and anchoring of the metal nanoparticles on NCF is evident from both microscopic (Fig. 1b-c) and spectroscopic (Fig. 1h-j) results. The TEM images of the samples confirm the stability of NCF matrix, that is now uniformly decorated with monodisperse metal nanoparticles. The representative TEM and SEM images recorded on Ag-Au-NCF-10 samples exhibit extensive alloying of Ag and Au, along with their robust interface with the disordered surface of NCF (Fig S4-S6). The crystalline

nature of Ag-Au nanoparticles and their uniform alloying is evident from the HAADF, EDS mapping (Fig S7-S8), and SAED pattern that clearly exhibits the (2 0 0), (1 1 1) and (3 1 1) crystal planes that arise due to alloying between Au and Ag (Fig. 1d-f) [72]. In addition, PXRD confirms the successful growth of Ag, Au and Ag-Au nanoparticles on the surface of NCF by the presence of characteristic diffraction peak with 2θ value $38.1°, 44.3°, 64.4°$ and $77.4°$ (Fig. S9-S11) [73]. The high propensity for surface oxidation in silver is reflected in the X-ray photoelectron spectra of both Ag-NCF-10 and Ag-Au-NCF-10 samples. Accordingly, the XPS of Ag 3d region in both these samples exhibits $3d_{3/2}$ (375.0 and 373.1 eV) and $3d_{5/2}$ (368.6 and 367.1 eV) peaks corresponding to both Ag^0 and Ag^{1+} oxidation states, respectively in Fig. 1h [74]. No such features corresponding to surface oxidation is observed in Au 4f peaks exhibited by Au-NCF-10 and Ag-Au-NCF-10 samples (Fig. 1i-j). Furthermore, the Ag-Au-NCF-10 hybrid exhibits a higher percentage of surface oxidized Ag compared to Ag-NCF-10 sample. This is attributed to the reduction of Au^{3+} to Au^0 by the photothermally reduced Ag^0, leading to greater oxidation of Ag^0 to Ag^{1+}. The combination of surface Ag^{+1} and Au^0 immobilize on NCF would be effective in minimizing in ohmic losses and greater confinement of electromagnetic fields. Since NCF has been established as a near-perfect blackbody absorber in our earlier works [75,76], we do not observe the characteristic surface plasmon absorbance of metal nanoparticles in the absorption spectra of Ag-NCF, Au-NCF and Ag-Au-NCF nanohybrids. Such a combination of NCF as the broadband absorber and plasmonic nanostructures is expected to serve as an excellent SPCE platform. This is validated by the excellent absorption of the electromagnetic spectrum (300–900 nm) for all the samples prepared (Fig. 1k). Since all the metal-NCF hybrids are fabricated through a photothermal reduction strategy, it becomes imperative to understand the role of exposure time in controlling the dynamics of nanoparticle formation. Accordingly, increase in the duration of solar illumination brings about a corresponding increase in the average size of the metal nanoparticles, as seen from the TEM images and their corresponding histograms (Fig. S12). Evidently, the photoreduction and subsequent immobilization of the metallic nanostructures on the surface of NCF increases with the time of solar exposure. However, extended periods of solar exposure (>10 min) causes Ostwald oxidative ripening leading to marginal changes in the particle dimensions. Therefore, we note that the growth of metal nanoparticles reaches saturation after 10 min of solar exposure (Fig. 1g).

4.2. Tunable SPCE enhancements using different NCF-metal hybrid variants

The strong absorption and the extensive metal-dielectric interface created in the metal-NCF hybrids through this strategy offers an excellent opportunity for their utilization as SPCE substrates. Since metal nanoparticles based plasmonics and nanostructured carbon-based dielectrics operate on fundamentally differing pathways, the extensive interface created in metal-NCF hybrids warranted a systematic study into their effectiveness as SPCE platform. Accordingly, we employed three different configurations (Fig. 2a), namely.

(a) Spacer configuration, with the polymer mediating the interaction between the radiating dipole of fluorophore with the metal-NCF hybrid.

(b) Cavity configuration, providing direct interaction between the radiating dipole of fluorophore with the metal-NCF hybrid, and.

(c) Extended cavity (ext. cavity), were in fluorophore is trapped between metal-NCF hybrid and Ag film.

These three configurations represent three contrasting environments for interaction of the fluorophore with the SPCE enhancers [29,30]. The synthesized metal-NCF hybrids were juxtaposed over the propagating surface plasmon polaritons of the metallic thin film in order to comprehensively understand the photo-plasmonic coupling efficiency. In spacer configuration, metal-NCF hybrid is pre-mixed with PVA solution and was spin-coated on SPCE substrate, followed by the deposition of RhB solution. Hence, the interaction between the fluorophore and the
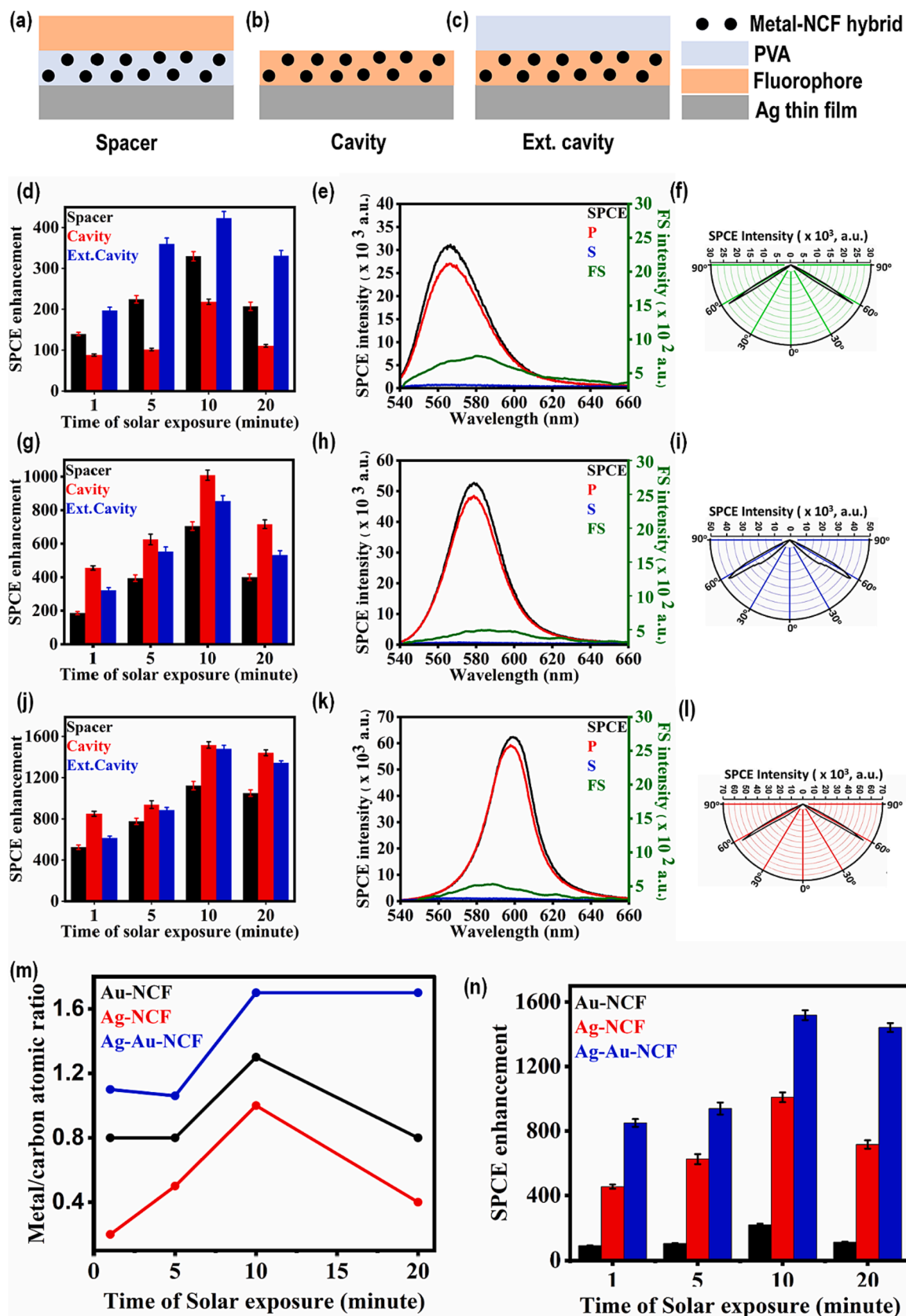
Fig. 2. Schematic representations of different SPCE interfaces investigated (a) spacer, (b) cavity and (c) ext. cavity. Variations in SPCE enhancements obtained with (d) Au-NCF, (g) Ag-NCF and (j) Ag-Au-NCF with the time of solar irradiation. SPCE, P, S and FS spectra and the corresponding angularity plot for the (e, f) Au-NCF-10 in ext.cavity, (h, i) Ag-NCF-10 in cavity and (k, l) Ag-Au-NCF-10 in cavity. (m) SPCE enhancement in cavity interface obtained with Au-NCF, Ag-NCF and Ag-Au-NCF nanohybrids synthesized using varying time of solar exposure, (n) Metal/Carbon atomic ratio in all nanohybrids as a function of solar exposure time.

dielectric material is mediated by the polymer. In comparison, the cavity configuration provides direct coupling between the fluorophore and the dielectric and is fabricated by mixing of RhB with the metal-NCF hybrid and PVA. The third configuration employs PVA as the bridging polymer to extend the coupling between the fluorophore and metal-NCF hybrid and is therefore referred to as ext. cavity. Thus, these three configurations, along with the variations of metal-NCF hybrids, act as a versatile model system to derive fundamental insights leading to the advancement of SPCE based analytical detection platforms. The microscopy images of such SPCE films, prepared with the metal-NCF hybrids shows uniform and continuous film formation in both optical microscopy and electron microscopy (Fig S13). Furthermore, the cross-sectional SEM images exhibit smooth and continuous morphology of the SPCE film. The SEM images recorded at lower magnification shows the impregnation of the Ag-Au-NCF into the polymeric film, that is also uniformly distributed over the substrate. The thickness of such films, is estimated from both cross-sectional SEM and optical microscopy to be 30–50 nm.

Accordingly, a matrix of devices (Fig. 2a-c) with varying metal-NCF hybrids prepared under different conditions of solar irradiation were evaluated for the magnitude of SPCE enhancements. Intriguing scientific understanding can be drawn from the observed trend in the SPCE enhancements. Irrespective of the device configuration, all three metal-NCF hybrids (Au-NCF, Ag-NCF, and Ag-Au-NCF) exhibits monotonic increase in SPCE enhancements with increasing time of solar irradiation. This trend continues up to 10 min of solar irradiation, following which there is a decline in the SPCE enhancements (Table S1). This is attributed to the increase in the size of the metal nanoparticles forming the metal-NCF hybrids beyond 10 min of solar exposure, which in turn results in dielectric mismatch between the active layer and the Ag thin film, in line with our earlier works [50]. Accordingly, we arrived at an optimum time interval of 10 min for obtaining the finest number of plasmonic hot-spots supporting high SPCE enhancements.

Based on these observations, the SPCE enhancements provided by Au-NCF-10, Ag-NCF-10, and Ag-Au-NCF-10 were directly compared in spacer, cavity and ext. cavity nanointerfaces (Fig. 2d, g, j). Through such experiments, Au-NCF-10 performed best in ext. cavity configuration in contrast to Ag-NCF-10 and Ag-Au-NCF-10, both of which gave the highest SPCE enhancements in cavity configuration. Quantitatively, the order of SPCE enhancements follows Ag-Au-NCF-10 (cavity) > Ag-NCF-10 (cavity) > Au-NCF-10 (ext. cavity). The Ag-Au-NCF and the fluorophores are located in differing electromagnetic environments in the cavity and extended cavity configurations. While the cavity configuration provides a direct coupling between the radiative dipoles of RhB with the near-field electromagnetic enhancement provided by Ag-Au-NCF, the extended cavity sandwiches the RhB between the Ag-Au-NCF and metal thin film. Thus, the fluorophore trapped between the Au-NCF and metal thin film in the extended cavity configuration is able to effectively experience the enhanced electromagnetic field in such sandwich configuration. However, it is to be noted that the absolute magnitude of SPCE enhancements obtained with Ag-Au-NCF in cavity configuration is always higher due to the direct enhancement of PMD. The lower enhancements obtained with Au-NCF hybrids is primarily on account of the quenching phenomena, in line with earlier studies utilizing RhB as fluorophore with Au NPs [77,78]. This is further substantiated by the Au-NCF providing the least SPCE enhancements in cavity nanointerfaces due to the dominant quenching effect arising from the direct admixture of Au-NCF with RhB. Thus, the Au-NCF nanohybrid works best in ext. cavity interface on account of its architectural design that enables the optimum combination of both spacer (material and dye-doped in separate nanolayers) and cavity (the dye molecules experience the electromagnetic hot-spots) nanointerfaces.

Importantly, the SPCE enhancements with Ag-Au-NCF-10 in both cavity and ext. cavity were estimated to be 1517-fold and 1480-fold and represent the highest obtained with any combination of metal-dielectric hybrids reported thus far. This is significantly outperforming several other plasmonic and non-plasmonic SPCE platforms such as low

dimensional carbon with Ag, Au, Ag-Au hybrids [33,35,79], metal-dielectric nanohybrids [36], Soret nanoparticle assemblies [80] and ceramic composites [81], reported earlier and constitutes an exclusive system delivering over three orders of magnitude enhancements in SPCE. The primary reason for this outcome lies in the morphological structure of the NCF that presence conducive mesoporous morphology mimicking conical microcavities and thereby facilitates extensive interface [50]. The superior SPCE enhancement achieved with Ag-Au-NCF is attributed to the optical cavitating effect of NCF, wherein the dielectric-based optical microscale cavities of NCF acts to confine the electromagnetic field and thereby enhance the SPCE enhancements. In brief, the NCF constitutes a large number of nano-curvatures and nano-vortices that result in the formation of uniformly distributed three-dimensional nanogaps sustaining high gradient of EM field intensity. The hierarchical anchoring of Ag and Au nanostructure on such structurally graded morphologies result in generation of high density of electromagnetic hot-spots, generating void plasmons. On account of its intensely interconnected nanogap architecture, the gap-plasmons specially overlap with the adjacent hybrids thereby generating partially propagating delocalized electron cloud density. The architectural design of cavity nanointerface allows the radiating dipoles to occupy such graded nanovoids and nano-curvatures, as a result of which the emission from such molecules undergo multiplicative effect. It is important to note that, although such collective and coherent photon scattering is expected in the case of Ag-NCF, Au-NCF, and Ag-Au-NCF nanohybrids. The surface-induced quenching in the case of Au-NCF outperforms the enhancement channels. Consequently, this photon cascading effect in cavity nanointerface results in drastically high SPCE enhancements in Ag-NCF and Ag-Au-NCF.

Lakowicz and co-workers pioneered surface plasmon-coupled emission (SPCE) technology as an effective biosensing platform where the fundamental understanding of the functionality of the substrates with mechanism of enhanced fluorescence are elucidated [30–32]. Here, the NPs present on metal thin film brings a synergistic combination of metal enhanced fluorescence (MEF) and surface plasmon-coupled emission (SPCE), on account of increased localized density of states. These unique nanoscale light-matter interaction within the SPCE platform have been utilized for detection of molecules and ions of biological and environmental interest at significantly low concentrations. In this context, this work describes the effective interfacing of Ag-Au-NCF nanohybrids over metallic thin films to drive the generation of high local field intensity due to augmented density of states, leading to enhanced fluorescence signal intensity and directionality of emission from proximaly located fluorophores.

At this juncture, it is worth noting that more than 1517-fold fluorescence enhancement is observed in cavity nanointerface with the use of Ag-Au-NCF-10, in spite of the possible contribution of Au towards emission quenching. In the context of several strategies utilized for obtaining Ag-Au heterometallic nanohybrid, our work demonstrates a single-pot fabrication of Ag-Au nanohybrid, by leveraging the photo-thermal properties of the porous nanocarbon framework. In accordance with earlier work [50], such nano-engineering results in the successful formation of heterometallic Au-Ag-Au plasmon passages that are distributed discontinuously over the NCF. Consequently, the Ohmic losses observed in the case of both pristine Ag and pristine Au are significantly nullified in their combination. The significantly lowered losses operating at the metal-dielectric interface thereby contribute to the high SPCE enhancements obtained. The spectral data and angularity plots reaffirm the SPCE nature of emission enhancement observed (Fig. 2 e-f, h-I, k-l). In the context of this study, the coupling of the emitted photons from the fluorophores (RhB) with the hybrid modes generated by the metal-dielectric nanohybrid (Ag-Au-NCF) produces the enhancement of electromagnetic field intensity in the near-field region. Such field are subsequently confined within the nanocavities of Ag-Au-NCF nanohybrid, resulting in the enhancement of the intensity of emitted photons from the fluorophores. We refer to such coupling as

intra-metal-dielectric coupling. On the other hand, intra metal-dielectric coupling is used to describe similar interactions occurring between adjacently located Ag-Au-NCF particles. Such unprecedented 1517-fold SPCE enhancements may be attributed to the factors including.

(a) hybrid intra-plasmonic coupling between the metallic NPs within Ag-Au-NCF nanohybrid.
(b) intra-metal-dielectric coupling between the metallic NPs and the NCF in a single Ag-Au-NCF nanohybrid.
(c) inter-plasmonic coupling between the metallic NPs of neighboring Ag-Au-NCF nanohybrids.
(d) inter-plasmonic heterometallic Ag-Au-dielectric NCF coupling between neighboring Ag-Au-NCF nanohybrids.
(e) Multiple total-internal scattering induced coupling of void plasmons sustained by the NCF corrugated morphologies, and.
(f) coupling between the Ag-Au-NCF nanohybrids and their individual components with the propagating plasmons of metallic thin film.

It becomes important to understand the role of metal loading and the metal-NCF ratio in determining the SPCE enhancements obtained (Fig S14). Accordingly, the SPCE enhancements obtained in cavity configuration were compared for all the three (Ag-NCF, Au-NCF and Ag-Au-NCF) prepared under varying time of solar illumination (Fig. 2m). It is observed that Au-NCF hybrid provided the least enhancement, irrespective of the metal-NCF ratio. This is expected, since the Au nanoparticle are established to be effective quenchers of SPCE enhancements [48,77]. On the other hand, the combination of Au and Ag, as present in Ag-Au-NCF nanohybrid provided the maximum enhancements, irrespective of the time of solar illumination. A strong direct correlation

between the SPCE enhancements obtained with Ag-Au-NCF nanohybrids to the metal–carbon ratio is observed (Fig. 2n). The highest SPCE enhancements were obtained at a metal–carbon ratio of 1.6 in Ag-Au-NCF, corresponding to 10 min of solar exposure. Further solar illumination is not observed to change this ratio and therefore has minimal effect on the SPCE enhancements also. This optimal metal–carbon loading, along with the Ag-Au alloy formed within the nanocavities of NCF, is therefore critical for achieving high SPCE enhancements. This also corresponds to larger size of the Ag-Au nanoparticles (mean diameter $\sim 15.6 \pm 0.36$ nm) that is in good agreement with the cavity dimensions of NCF.

In light of these observations, our route to generate metal-dielectric hybrids is therefore expected to have widespread implications for rapid, user-eco-friendly technology for large-scale production of nanohybrid libraries by tuning the metal ion of interest. Importantly, we leverage the unprecedented and high SPCE enhancements provided by Ag-Au-NCF-10 to demonstrate powerful and environmentally relevant, ultra-sensitive analytical detection.

4.3. Sensing of PFOS and PFOA

The extraordinary SPCE enhancements (1517-fold) achieved with Ag-Au-NCF-10 nanohybrid in cavity configuration presented a unique opportunity for employing this platform towards ultrasensitive and reliable detection of environmental contaminants. Accordingly, we set out to monitor the emerging and hazardous class of fluoro compounds such as PFOS and PFOA [5], with the aim of devising a portable SPCE detection system. Our choice of analytes was dictated by their (a) spectroscopic and electrochemical 'silent' character, (b) accumulative and persistent nature of PFAS, warranting its early-stage detection at ultra-low concentrations, (c) emerging ubiquities in water and soil
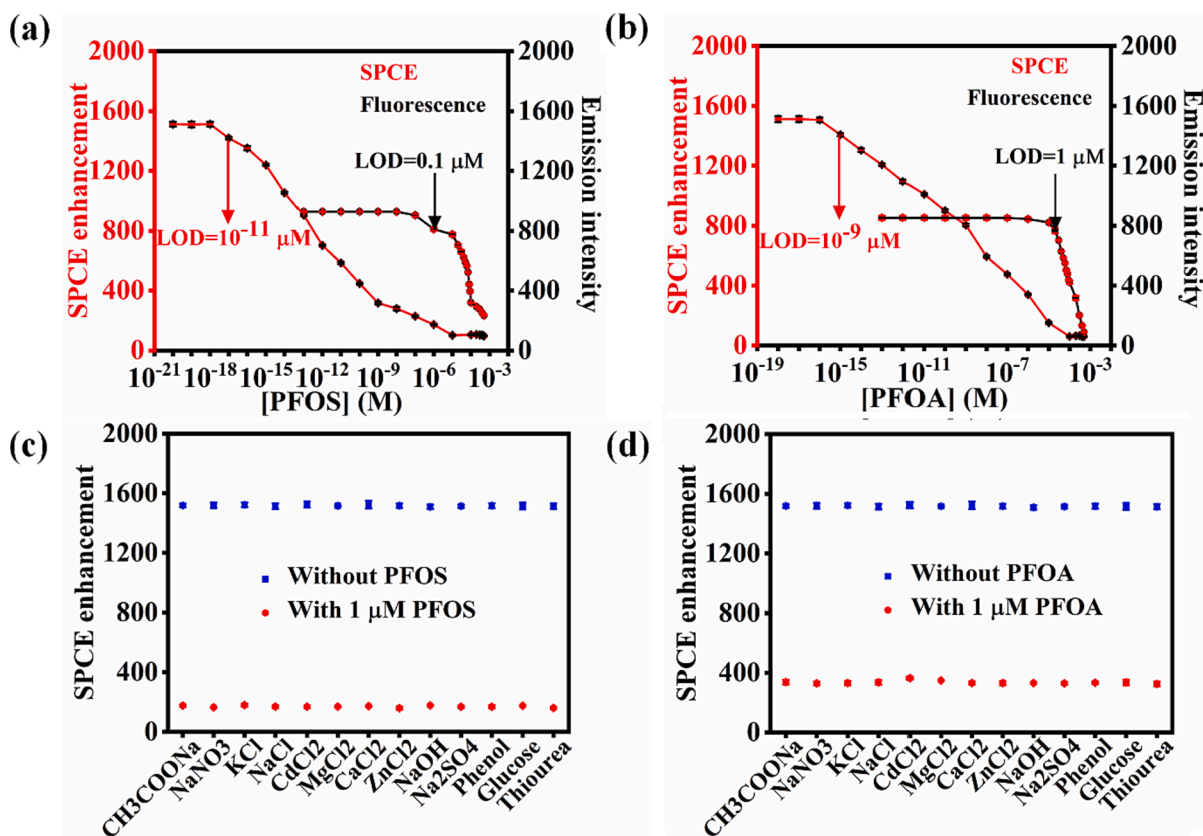

Fig. 3. Comparison of SPCE enhancement (red) and conventional fluorescence intensity (black, absolute) with varying concentrations of (a) PFOS and (c) PFOA. (b) Comparison of SPCE enhancements obtained without PFOS (blue) and with 1 μM PFOS + 100 μM interferons (red). (d) Comparison of SPCE enhancements obtained without PFOA (blue) and with 1 μM PFOA + 100 μM interferons (red). (For interpretation of the references to color in this figure legend, the reader is referred to the web version of this article.). (For interpretation of the references to color in this figure legend, the reader is referred to the web version of this article.)

leading to sever environmental and health hazards and (d) current lack of real-time, field deployable detection solutions. Accordingly, the SPCE device consisted of admixed Ag-Au-NCF-10, RhB and fluoro-contaminant (PFOS or PFOA) in cavity configuration.

The magnitude of SPCE enhancements was found to systematically decrease with increasing concentration of the analyte (PFOS or PFOA) (Fig. 3. a-b, Fig. S15). Importantly, the change in SPCE enhancements was measurable and reliably quantifiable starting from 10^{-17} M of PFOS (5×10^{-3} ppt) and 10^{-15} M of PFOA (4.14×10^{-1} ppt). It is important to note that this detection limit ranging from $10^{-15} - 10^{-17}$ M corresponds to detection at single molecular levels. Thereby, this report constitutes the first in our knowledge to achieve single molecular level detection of fluoro compounds. Furthermore, the relative standard deviation (RSD) of 9.67 % for PFOS and 2.2 % for PFOA, confirms the robustness and reliability of this detection platform. Moreover, the decrease in SPCE enhancements exhibits a monotonic trend till a concentration of 10^{-5} M for PFOS and 10^{-4} M for PFOA, thereby achieving an effective operational range of 10^{10} for PFOS and 10^{8} for PFOA. The linearity of response across such a wide operational range spanning 8–10 orders of magnitude, along with the large sensitivity associated with the signalling (PFOS = 155.78 counts, PFOA = 144.98 counts) and reliability of response (RSD = 9.67 % and 2.2 respectively for PFOS and PFOA) is unprecedented for both PFOS and PFOA. Interestingly, such high-performance metrics also presents new landscape for evolving novel SPCE-based detection platforms. This originates primarily due to the rational design principles developed for realizing 1517-fold emission enhancements by synergistic tailoring of plasmonic and dielectric electromagnetic field confinement in Ag-Au-NCF-10.

It is imperative to assess the specificity of any sensible analytical detection that operates at such low concentrations of analytical detection. Accordingly, SPCE enhancements provided by Ag-Au-NCF-10 platforms in the presence of 1 µM each of PFOS and PFOA were estimated in the presence of 100-fold higher concentrations of thirteen different potential interferons (CH_3COONa, $NaNO_3$, KCl, NaCl, $CdCl_2$, $MgCl_2$, $CaCl_2$, $ZnCl_2$, NaOH, Na_2SO_4, Phenol, Glucose, Thiourea) [9]. These interferons belong to a wide range of chemical libraries consisting of ionic, organic, water-soluble, and biodegradable compounds. Screening of these interferons was carried out on the basis of their shared origin with fluoro compound and their dominant presence in potential water sources. Significantly, none of these thirteen potential interferons provides any noticeable or quantifiable change in the SPCE enhancement intensities (Fig. 3. c-d). Thus, the quenching of SPCE enhancements corresponds exactly to that obtained with pristine PFOS and PFOA and thereby establishes the extreme specificity of interaction between the SPCE platform and analyte leading to the signalling. Additionally, we attempted to carry out SPCE experiments with 4-nitrobenzenesulfonyl chloride and 4-amino-3-hydroxynaphthalene-1-sulfonic acid as potential interferons with PFOS, due to the shared sulfate groups. However, both these chemicals were insoluble in water, even at ppm levels, and therefore did not provide reliable results for detection.

Control experiments monitoring the fluorescence quenching of RhB with PFOS and PFOA was ineffective below concentration of 10^{-7} M and 10^{-6} M, respectively (Fig. S16 and S17). This constitutes a 1000 times higher concentration than the WHO stipulated limit (70 ppt) [7] and importantly establishes that direct fluorescence quenching of RhB by PFOS and PFOA is ineffective at these relevant and critical concentrations. In addition, the specificity of response achieved warrants further fundamental understanding of the interaction between RhB and PFAS. Accordingly, the lifetime measurements on RhB + PFAS was carried out through fluorescence lifetime imaging microscopy (FLIM). While pristine RhB exhibits a mono-exponential decay with a lifetime of 3.65 ns, the decay profile changes to a bi-exponential character with a lifetime of 1.17 ns and 2.73 ns due to the addition of PFOS. Identical trends with biexponential decay (3.30 ns, 1.49 ns) are obtained with PFOA, confirming the similarity of their interaction with RhB (Fig. S18) [50,82].

Complimentary experiments accessing the zeta potential of pristine RhB and its combination with PFAS were carried out. Consistent with the fluorescence measurements, a significant lowering in the zeta potential of RhB is observed in the presence of both PFOS and PFOA (Table S2). These results taken together, implies a charge-transfer based interaction between the fluorophore (RhB) and analyte (PFOA/PFOS). Such a hypothesis is augmented by detailed theoretical calculations that is presented in the subsequent section.

Density Functional Theoretical calculations were performed using hybrid B3LYP functional employing the Gaussian 16 suite to understand the interaction between the RhB, PFOS, and PFOA. To begin with, RhB and PFOS/PFOA are optimised together (Fig. 4). This stable optimised structure yielded a binding energy of -372 kJmol^{-1} and -340 kJmol^{-1} for PFOS and PFOA, respectively. Such a strong binding affinity is attributed to a strong interaction between the two molecules, and hence the optimised geometries are further analysed. Our analysis reveals that the SO_3^- (sulfonate) and CO_2^- (carboxylate) groups of PFOS and PFOA, respectively, are located in close proximity to the $N(CH_2CH_3)^+$ (ammonium) group of RhB (3.1 Å –3.9 Å) (Fig. 4), indicating the occurrence of cation–anion interactions. Furthermore, we observe the formation of hydrogen bonds between the hydrogen atom of the carboxylic group in RhB and the O^- atom of the sulfonate group (1.7 Å), and the O^- atom of the carboxylate group (1.6 Å) in PFOS and PFOA, respectively. Additionally, we performed another set of calculations involving 4-Chlorobenzenesulfonate with RhB (Fig. S19). DFT computed geometry revealed a significant binding energy of -344 kJ/mol, indicating favourable interactions between RhB and sulfonic acids other than PFOS and PFOA.

An intriguing observation that can be drawn from such an analysis is the deviation from planarity in RhB when exposed to acids. The aromatic structure in RhB exhibits a notable bending from planarity by approximately 5°. This alteration in the molecular geometry adds an exciting dimension to the behaviour of RhB in the presence of acids, given that the absorption in chromophores relies heavily on planarity. To understand the interactions between RhB and acids, we performed an Atoms in Molecules (AIM) analysis. The nature of the Bond Critical Point (BCP) was determined using the $|V(r)/G(r)|$ ratio (Fig. S20, S21 and Table S3, S4). If the $|V(r)/G(r)|$ ratio is between 0 and 1, it indicates predominantly ionic interactions. The ratio between 1 and 2 suggests intermediate interactions, while ratios greater than 2 suggest covalent interactions. We thoroughly analysed all the BCP between the two entities, and they consistently indicated an ionic nature of the interaction (see Table S3 in supplementary file). This analysis further confirms the presence of cation–anion-type interactions (Fig. 4, Fig. S20, S21).

Further TDDFT calculations were performed to understand the nature of the observed transition and probe the origins of quenching. While none of the exchange–correlation functionals is illustrated to accurately reproduce the vertical excitation energies of the RhB, among tested functionals, BP86 was found to yield a good trade-off, which has been used in our case [83]. Our calculations suggest a strong π-π* feature centered at ~ 478 nm for RhB (Fig. S22-S24). Upon interaction with the PFOS (PFOA), this feature was found to be red-shifted to 500 nm (506 nm) with a shoulder detected at 462 nm (449 nm) that corresponds to another π-π* transition (Fig. S22-S24). This shift that is observed due to the interaction with the PFOS and PFOA to lower energy is due to the aforementioned non-covalent interactions. Particularly strong anion…π interactions stabilise the corresponding π* orbitals leading to a relatively smaller π-π* gap and hence the shift that facilitates the quenching (Fig. S25-S26).

4.4. Real-time field tests

Utilizing the strengths of the SPCE detection platform, we demonstrate its field testing for detection of PFAS from various environmental and biological sources. Since PFAS has extreme chemical stability, its presence in various water bodies and subsequent penetration to the
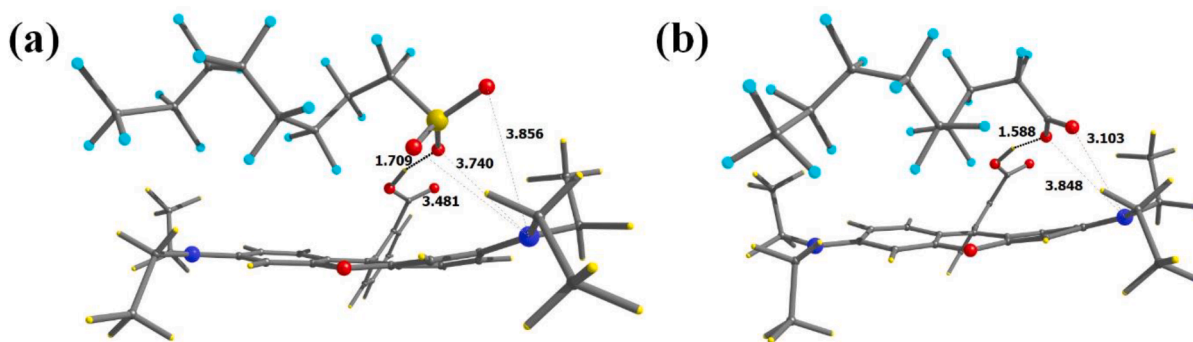
Fig. 4. DFT optimized structure of (a) RhB-PFOS (b) RhB-PFOA showing the interactions between two. Colour Code: C-grey, F-cyan, O-red, N-blue. (For interpretation of the references to color in this figure legend, the reader is referred to the web version of this article.). (For interpretation of the references to color in this figure legend, the reader is referred to the web version of this article.)
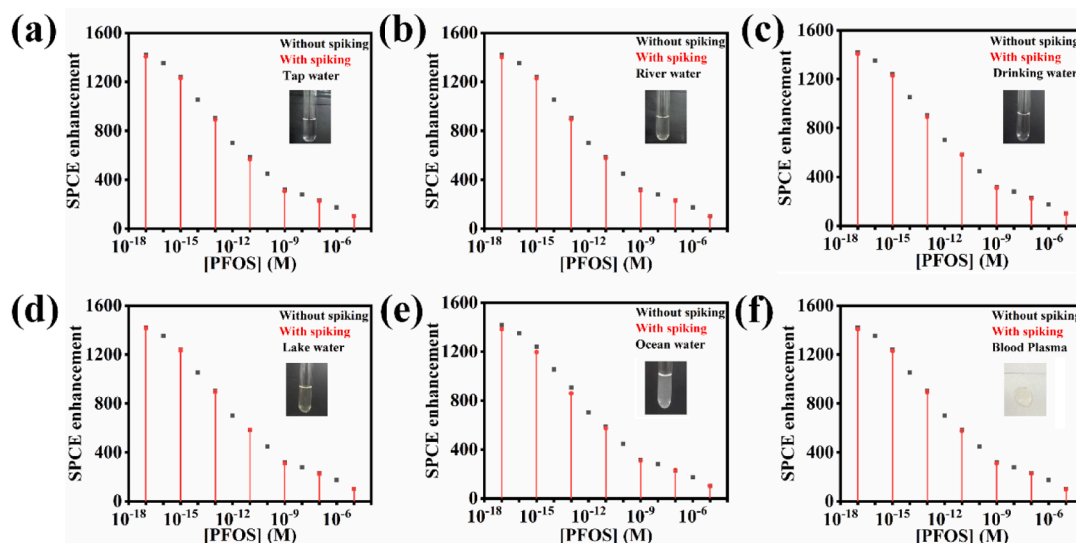

Fig. 5. Comparison of SPCE enhancements obtained without spiking (black) and with spiking (red) for different samples containing PFOS such as (a) tap water (b) river water (c) drinking water (d) lake water (e) ocean water (f) blood-plasma. Photographs of the corresponding samples are given as inset. (For interpretation of the references to color in this figure legend, the reader is referred to the web version of this article.). (For interpretation of the references to color in this figure legend, the reader is referred to the web version of this article.)

human food chain has been an increase in cross of concern. Accordingly, we drew samples from five different water bodies namely tap water, river water (Chitravathi, Andrapradesh, India), drinking water, lake water (Powai Lake, Maharashtra, India) and ocean water (Juhu Chowpatty Beach, Maharashtra, India) and artificially spiked them with varying concentrations of PFOS and PFOA (Fig. 5a-e and Fig. 6a-e). In addition, blood plasma was also spiked with identical concentrations of PFOS and PFOA for comprehensive field testing (Fig. 5f and Fig. 6f) . Significantly, the quantification from lab scale experiments were exactly validated through this field-testing trial with an 100 % agreement between the SPCE enhancements obtained in lab scale and those obtained during the field testing. The excellent correlation between these values confirm the potential ability of the SPCE based technique to monitor the analysis of PFOS and PFOA. This technique can be extended as a new strategy for the detection of PFOS and PFOA in common detection system.

All the sensing studies were performed using cost-effective smartphone-based detector as a replacement for the current state-of-art complex, bulky and expensive readout systems. Such approaches that aid in decentralization of the laboratory-confined biosensing technologies are gaining increased interest in disease diagnostics as well as for monitoring the quality and safety of environmental bodies (air, water, and soil). Especially, the smartphone-based healthcare management

systems are significantly researched due to their low-cost, portability, superior cameras and memory storage capability, ever-advancing software, and hardware accessories with auxiliary benefit of cloud computing and association with distant physicians or health experts for immediate feedback. In this context, the images of the SPCE were captured using a smartphone and processed using the ColorGrab app. The luminosity values obtained from the smartphone images during the sensing of PFOS/PFOA is plotted in the right y-axis with respect to the SPCE enhancement (Fig. 7a, c & Fig. S27). It is observed that there is an excellent correlation between the luminosity values and the SPCE enhancements (Ocean Optics detector), thereby enabling smartphone-based sensing in a reliable and reproducible manner. The color cards and processed image corresponding to the different addition of PFAS were presented in Fig. 7b and 7d respectively for PFOS and PFOA enabling visual detection and quantification of the PFAS using smartphone (Fig. S28-29).

Finally, we benchmark the ultra-high sensitivity, specificity and ease of detection of a particularly challenging and rapidly emerging environmental contaminant (PFAS) with global WHO recommendations and several other studies drawn from the literature [3,14–18,84–91] (Fig. 8). The platform integrated with mobile phone demonstrates the first visual detection of fluoroalkyl contaminants at unprecedented sensitivity that is three orders of magnitude lower than the limit set by WHO (Fig. 8a).
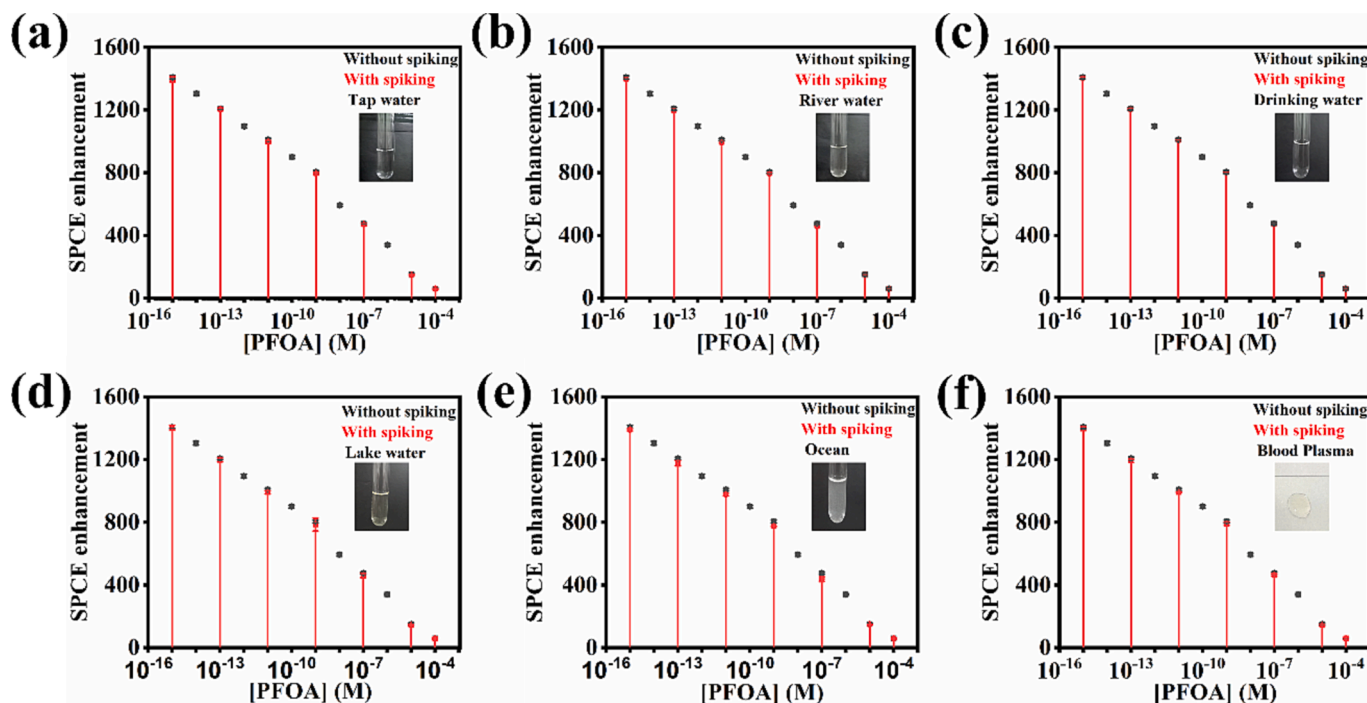
Fig. 6. Comparison of SPCE enhancements obtained without spiking (black) and with spiking (red) for different samples containing PFOA such as (a) tap water (b) river water (c) drinking water (d) lake water (e) ocean water (f) blood-plasma. Photographs of the corresponding samples are given as inset. (For interpretation of the references to color in this figure legend, the rea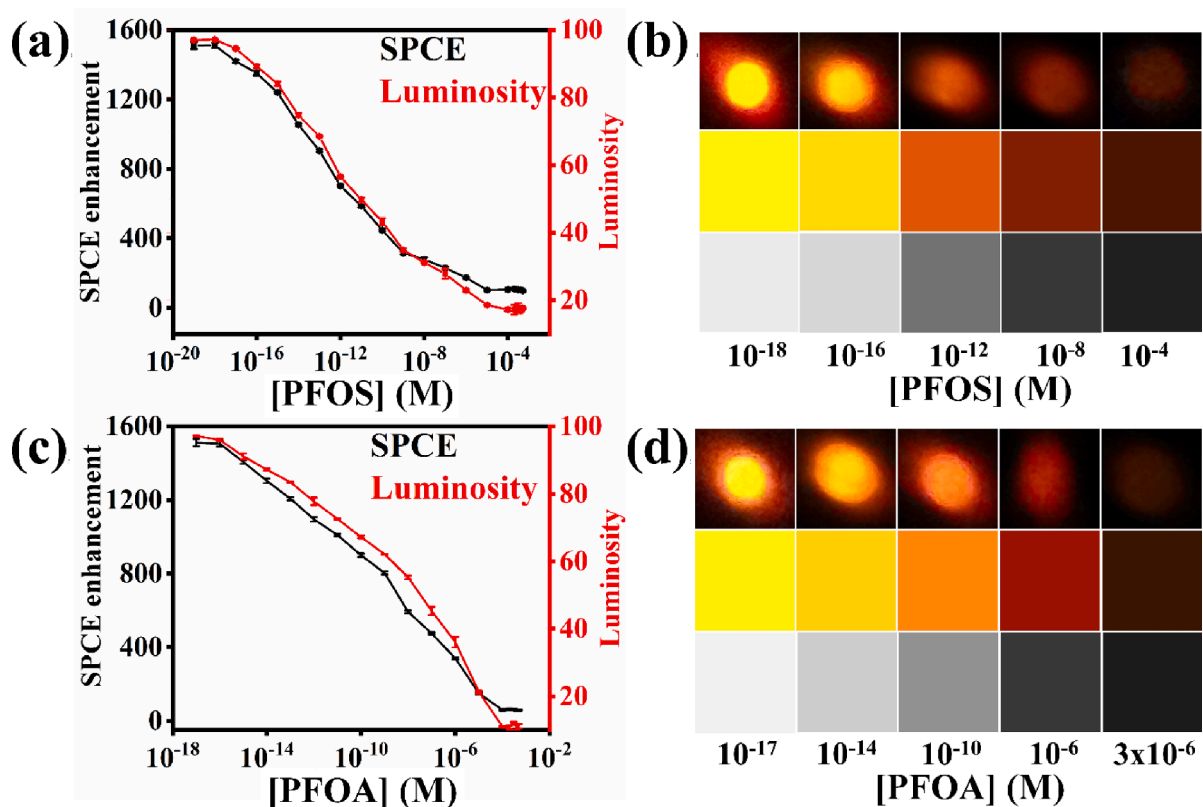der is referred to the web version of this article.). (For interpretation of the references to color in this figure legend, the reader is referred to the web version of this article.)

Fig. 7. SPCE enhancements and their corresponding luminosity values obtained using mobile phone camera-based detection, along with color cards and processed images, respectively for (a, b) PFOS, (c, d) PFOA.
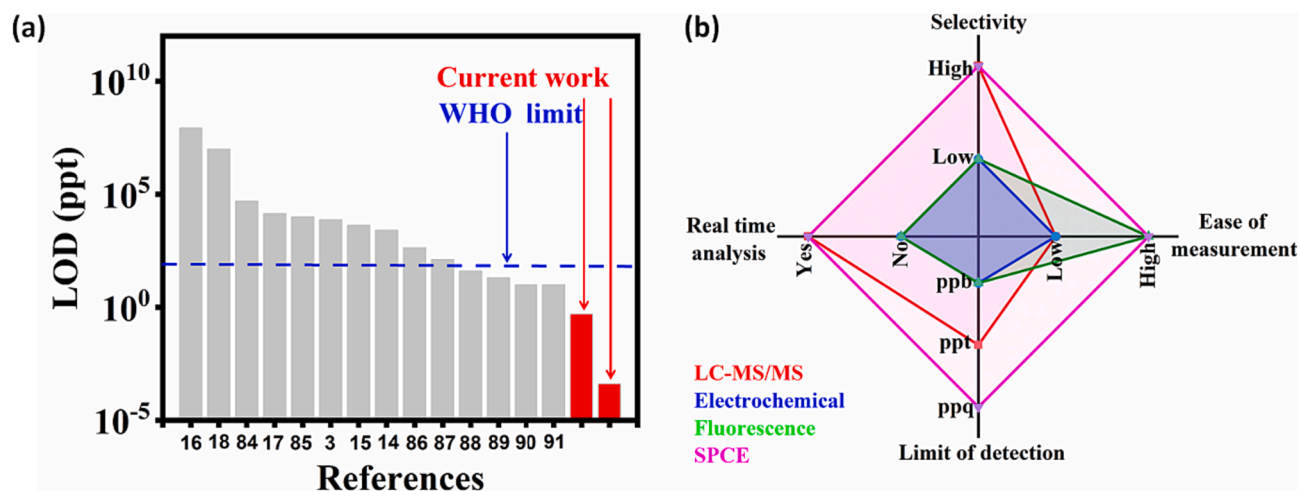
Fig. 8. Comparison of LOD of our method with different reported techniques and (b) Spider plot illustrating qualitative evaluation of the performance of various PFAS sensors based on their real-time analytical capability, sensitivity, LOD, and ease of measurement.

These results assume immense technological relevance given the persistent and accumulative nature of PFAS. Such a comparison highlights the importance of this work in achieving outstanding performance in detection while simultaneously complying with the stringent demands of real-time sampling along with reliable on-field deployability (Fig. 8b).

5. Conclusion

In summary, we establish nanoengineered metal-dielectric hybrids as excellent platforms for obtaining one of the highest reported SPCE enhancements (1517-fold). While the bimetallic Ag-Au alloy synergises to lower the Ohmic losses, subsequent coupling with nanocarbon-based dielectric contributes to high PMD through broadband absorption and cavity-based confinement of the electromagnetic field intensities. Such unprecedented enhancements achieved have been leveraged for robust and reliable single-molecular level detection of fluorinated alkyl-compounds. The utility of such detection is extended beyond lab to practical, on-field samples drawn from various sources, with signal detection being achieved with a smartphone camera.

CRediT authorship contribution statement

Dipin Thacharakkal: Conceptualization, Investigation, Formal analysis, Data Curation, Methodology, Writing- original draft, Writing-review and editing, Validation. **Seemesh Bhaskar:** Conceptualization, Investigation, Formal analysis, Methodology, Writing- original draft, Validation. **Tanu Sharma:** Software, Investigation, Formal analysis, Methodology, Writing – original draft, Validation. **Gopalan Rajaraman:** Conceptualization, Methodology, Validation, Writing – review and editing, Supervision, Funding acquisition, Resources. **Sai Sathish Ramamurthy:** Conceptualization, Methodology, Validation, Writing – review and editing, Supervision, Funding acquisition, Resources. **Chandramouli Subramaniam:** Conceptualization, Data Curation, Formal analysis, Methodology, Validation, Writing – review and editing, Supervision, Project administration, Funding acquisition, Resources

Declaration of competing interest

The authors declare that they have no known competing financial interests or personal relationships that could have appeared to influence the work reported in this paper.

Data availability

Data will be made available on request.

Appendix A. Supplementary data

Supplementary data to this article can be found online at https://doi.org/10.1016/j.cej.2023.148166.

References

[1] H. Viberg, P. Eriksson, EPA fact sheet US, in: Reprod. Dev. Toxicol., Elsevier, 2011, pp. 623–635, https://doi.org/10.1016/B978-0-12-382032-7.10047-5.

[2] L. Jane, L. Espartero, M. Yamada, J. Ford, G. Owens, T. Prow, A. Juhasz, Health-related toxicity of emerging per- and polyfluoroalkyl substances: Comparison to legacy PFOS and PFOA, Environ. Res. 212 (2022), 113431, https://doi.org/10.1016/j.envres.2022.113431.

[3] N. Cennamo, G. D'Agostino, G. Porto, A. Biasiolo, C. Perri, F. Arcadio, L. Zeni, A Molecularly Imprinted Polymer on a Plasmonic Plastic Optical Fiber to Detect

Perfluorinated Compounds in Water, Sensors. 18 (2018) 1836, https://doi.org/10.3390/s18061836.

[4] J. Stone, P. Sutrave, E. Gascoigne, M.B. Givens, R.C. Fry, T.A. Manuck, Exposure to toxic metals and per- and polyfluoroalkyl substances and the risk of preeclampsia and preterm birth in the United States: a review, Am. J. Obstet. Gynecol. MFM. 3 (2021), 100308, https://doi.org/10.1016/j.ajogmf.2021.100308.

[5] E.M. Sunderland, X.C. Hu, C. Dassuncao, A.K. Tokranov, C.C. Wagner, J.G. Allen, A review of the pathways of human exposure to poly- and perfluoroalkyl substances (PFASs) and present understanding of health effects, J. Exposure Sci. Environ. Epidemiol. 29 (2019) 131–147, https://doi.org/10.1038/s41370-018-0094-1.

[6] D.Q. Andrews, O.V. Naidenko, Population-Wide Exposure to Per- and Polyfluoroalkyl Substances from Drinking Water in the United States, Environ. Sci. Technol. Lett. 7 (2020) 931–936, https://doi.org/10.1021/acs.estlett.0c00713.

[7] R. Khan, D. Andreescu, M.H. Hassan, J. Ye, S. Andreescu, Nanoelectrochemistry Reveals Selective Interactions of Perfluoroalkyl Substances (PFASs) with Silver Nanoparticles, Angew. Chem., Int. Ed. 61 (2022), https://doi.org/10.1002/anie.202209164.

[8] J. Yu, J. Hu, S. Tanaka, S. Fujii, Perfluorooctane sulfonate (PFOS) and perfluorooctanoic acid (PFOA) in sewage treatment plants, Water Res. 43 (2009) 2399–2408, https://doi.org/10.1016/j.watres.2009.03.009.

[9] Y. Wang, S.B. Darling, J. Chen, Selectivity of Per- and Polyfluoroalkyl Substance Sensors and Sorbents in Water, ACS Appl. Mater. Interfaces. 13 (2021) 60789–60814, https://doi.org/10.1021/acsami.1c16517.

[10] S. Garg, P. Kumar, G.W. Greene, V. Mishra, D. Avisar, R.S. Sharma, L.F. Dumée, Nano-enabled sensing of per-/poly-fluoroalkyl substances (PFAS) from aqueous systems – A review, J. Environ. Manage. 308 (2022) 114655, https://doi.org/10.1016/j.jenvman.2022.114655.

[11] Y.H. Cheng, D. Barpaga, J.A. Soltis, V. Shutthanandan, R. Kargupta, K.S. Han, B.P. McGrail, R.K. Motkuri, S. Basuray, S. Chatterjee, Metal-Organic Framework-Based Microfluidic Impedance Sensor Platform for Ultrasensitive Detection of Perfluorooctanesulfonate, ACS Appl. Mater. Interfaces. 12 (2020) 10503–10514, https://doi.org/10.1021/acsami.9b22445.

[12] Z. Zheng, H. Yu, W.-C. Geng, X.-Y. Hu, Y.-Y. Wang, Z. Li, Y. Wang, D.-S. Guo, Guanidinocalix[5]arene for sensitive fluorescence detection and magnetic removal of perfluorinated pollutants, Nat. Commun. 10 (2019) 5762, https://doi.org/10.1038/s41467-019-13775-1.

[13] B. Chen, Z. Yang, X. Qu, S. Zheng, D. Yin, H. Fu, Screening and Discrimination of Perfluoroalkyl Substances in Aqueous Solution Using a Luminescent Metal-Organic Framework Sensor Array, ACS Appl. Mater. Interfaces. 13 (2021) 47706–47716, https://doi.org/10.1021/acsami.1c15528.

[14] S. Chen, A. Li, L. Zhang, J. Gong, 13, Anal. Chim. Acta. 896 (2015) 68–77, https://doi.org/10.1016/j.aca.2015.09.022.

[15] H. Niu, S. Wang, Z. Zhou, Y. Ma, X. Ma, Y. Cai, 5, Anal. Chem. 86 (2014) 4170–4177, https://doi.org/10.1021/ac403406d.

[16] C. Fang, M. Megharaj, R. Naidu, Surface-enhanced Raman scattering (SERS) detection of fluorosurfactants in firefighting foams, RSC Adv. 6 (2016) 11140–11145, https://doi.org/10.1039/C5RA26114G.

[17] J. Liang, X. Deng, K. Tan, An eosin Y-based "turn-on" fluorescent sensor for detection of perfluorooctane sulfonate, Spectrochim. Acta, Part A 150 (2015) 772–777, https://doi.org/10.1016/j.saa.2015.05.069.

[18] Q. Chen, P. Zhu, J. Xiong, L. Gao, K. Tan, 4, Spectrochim, Acta, Part A. 224 (2020), 117362, https://doi.org/10.1016/j.saa.2019.117362.

[19] H. Ryu, B. Li, S. De Guise, J. McCutcheon, Y. Lei, Recent progress in the detection of emerging contaminants PFASs, J. Hazard. Mater. 408 (2021), 124437, https://doi.org/10.1016/j.jhazmat.2020.124437.

[20] S.K. Chaubey, D. Paul, S. Tiwari, A. Rahman, G.V.P. Kumar, Directional emission from tungsten disulfide monolayer coupled to plasmonic nanowire-on-mirror cavity, Adv. Photonics Res. 2 (2021) 2100002, https://doi.org/10.1002/adpr.202100002.

[21] C. Subramaniam, T.S. Sreeprasad, T. Pradeep, G.V. Pavan Kumar, C. Narayana, T. Yajima, Y. Sugawara, H. Tanaka, T. Ogawa, J. Chakrabarti, Visible fluorescence induced by the metal semiconductor transition in composites of carbon nanotubes with noble metal nanoparticles, Phys. Rev. Lett. 99 (2007), 167404, https://doi.org/10.1103/PhysRevLett.99.167404.

[22] S. Tiwari, U. Khandelwal, V. Sharma, G.V.P. Kumar, Single molecule surface enhanced raman scattering in a single gold nanoparticle-driven thermoplasmonic tweezer, J. Phys. Chem. Lett. 12 (2021) 11910–11918, https://doi.org/10.1021/acs.jpclett.1c03450.

[23] K.-X. Xie, Z. Li, J.-H. Fang, S.-H. Cao, Y.-Q. Li, Au-Ag alloy nanoshuttle mediated surface plasmon coupling for enhanced fluorescence imaging, Biosensors. 12 (2022) 1014, https://doi.org/10.3390/bios12111014.

[24] R. Rastogi, E.A. Dogbe Foli, R. Vincent, P.-M. Adam, S. Krishnamoorthy, Engineering electromagnetic hot-spots in nanoparticle cluster arrays on reflective substrates for highly sensitive detection of (bio)molecular analytes, ACS Appl. Mater. Interfaces. 13 (2021) 32653–32661, https://doi.org/10.1021/acsami.1c01953.

[25] Y. Huang, K. Dai, J. Zhang, G. Dawson, Photocatalytic CO2 conversion of W18O49/CdSe-Diethylenetriamine with high charge transfer efficiency: Synergistic effect of LSPR effect and S-scheme heterojunction, Chinese, J. Catal. 43 (2022) 2539–2547, https://doi.org/10.1016/S1872-2067(21)64024-X.

[26] N. Lu, X. Jing, Y. Xu, W. Lu, K. Liu, Z. Zhang, Effective cascade modulation of charge-carriers kinetics in the well-designed multi-component nanofiber system for highly-efficient photocatalytic H2 generation, Acta Phys. -Chim. Sin. 38 (2022) 2207045, https://doi.org/10.3866/PKU.WHXB202207045.

[27] X. Jiang, J. Huang, Z. Bi, W. Ni, G. Gurzadyan, Y. Zhu, Z. Zhang, Plasmonic Active "Hot Spots"-Confined Photocatalytic CO 2 Reduction with High Selectivity for CH 4 Production, Adv. Mater. 34 (2022) 2109330, https://doi.org/10.1002/adma.202109330.

[28] J. Peng, J. Shen, X. Yu, H. Tang, Q.L. Zulfiqar, Construction of LSPR-enhanced 0D/2D CdS/MoO3− S-scheme heterojunctions for visible-light-driven photocatalytic H2 evolution, Chinese, J. Catal. 42 (2021) 87–96, https://doi.org/10.1016/S1872-2067(20)63595-1.

[29] N. Lu, X. Jing, J. Zhang, P. Zhang, Q. Qiao, Z. Zhang, Photo-assisted self-assembly synthesis of all 2D-layered heterojunction photocatalysts with long-range spatial separation of charge-carriers toward photocatalytic redox reactions, Chem. Eng. Journal. 431 (2022), 134001, https://doi.org/10.1016/j.cej.2021.134001.

[30] J.R. Lakowicz, K. Ray, M. Chowdhury, H. Szmacinski, Y. Fu, J. Zhang, K. Nowaczyk, Plasmon-controlled fluorescence: a new paradigm in fluorescence spectroscopy, Analyst. 133 (2008) 1308, https://doi.org/10.1039/b802918k.

[31] J.R. Lakowicz, Radiative decay engineering 3. Surface plasmon-coupled directional emission, Anal. Biochem. 324 (2004) 153–169, https://doi.org/10.1016/j.ab.2003.09.039.

[32] I. Gryczynski, J. Malicka, Z. Gryczynski, J.R. Lakowicz, Radiative decay engineering 4. Experimental studies of surface plasmon-coupled directional emission, Anal. Biochem. 324 (2004) 170–182, https://doi.org/10.1016/j.ab.2003.09.036.

[33] A. Rai, S. Bhaskar, G. Kalathur Mohan, S.S. Ramamurthy, Biocompatible Gellucire ® Inspired Bimetallic Nanohybrids for Augmented Fluorescence Emission Based on Graphene Oxide Interfacial Plasmonic Architectures, ECS Trans. 107 (2022) 4527–4535, https://doi.org/10.1149/10701.4527ecst.

[34] V.S.K. Cheerala, K.M. Ganesh, S. Bhaskar, S.S. Ramamurthy, S.C. Neelakantan, Smartphone-based attomolar cyanide ion sensing using au-graphene oxide cryosoret nanoassembly and benzoxazolium-based fluorophore in a surface plasmon-coupled enhanced fluorescence interface, Langmuir. 39 (2023) 7939–7957, https://doi.org/10.1021/acs.langmuir.3c00801.

[35] K.M. Ganesh, A. Rai, S. Bhaskar, N. Reddy, S.S. Ramamurthy, Plasmon-enhanced fluorescence from synergistic engineering of graphene oxide and sharp-edged silver nanorods mediated with castor protein for cellphone-based attomolar sensing, J. Lumin. 260 (2023), 119835, https://doi.org/10.1016/j.jlumin.2023.119835.

[36] S. Bhaskar, P. Das, V. Srinivasan, S.B.N. Bhaktha, S.S. Ramamurthy, Plasmonic-Silver Sorets and Dielectric-Nd2O3 nanorods for Ultrasensitive Photonic Crystal-Coupled Emission, Mater. Res. Bull. 145 (2022), 111558, https://doi.org/10.1016/j.materresbull.2021.111558.

[37] S. Bhaskar, S.S. Ramamurthy, High Refractive Index Dielectric TiO 2 and Graphene Oxide as Salient Spacers for > 300-fold Enhancements, in: 2021 IEEE International Conference on Nanoelectronics, Nanophotonics, Nanomaterials, Nanobioscience & Nanotechnology (5NANO), IEEE, Kottayam, Kerala, India, 2021, pp. 1–6, https://doi.org/10.1109/5NANO51638.2021.9491131.

[38] C. Dreser, D.A. Gollmer, G. Bautista, X. Zang, D.P. Kern, M. Kauranen, M. Fleischer, Plasmonic mode conversion in individual tilted 3D nanostructures, Nanoscale. 11 (2019) 5429–5440, https://doi.org/10.1039/C8NR10254F.

[39] D. Wu, Y. Wang, Y. Liu, J. La, S. He, F. Lv, W. Wang, Bloch-Surface Plasmon Polariton Enhanced Amplified and Directional Spontaneous Emission from Plasmonic Hexagonal Nanohole Array, ACS Appl. Mater. Interfaces. 15 (2023) 16198–16203, https://doi.org/10.1021/acsami.2c22139.

[40] A.I. Maaroof, M.B. Cortie, N. Harris, L. Wieczorek, Mie and Bragg Plasmons in Subwavelength Silver Semi-Shells, Small. 4 (2008) 2292–2299, https://doi.org/10.1002/smll.200800203.

[41] N.H.T. Tran, K.T.L. Trinh, J.-H. Lee, W.J. Yoon, H. Ju, Reproducible Enhancement of Fluorescence by Bimetal Mediated Surface Plasmon Coupled Emission for Highly Sensitive Quantitative Diagnosis of Double-Stranded DNA, Small. 14 (2018) 1801385, https://doi.org/10.1002/smll.201801385.

[42] K.-X. Xie, R.-P. Huo, X.-L. Song, Q.-L. Liu, Y. Jiang, Y.-H. Li, L.-L. Dong, J.-X. Cheng, Fluorescence enhancement of surface plasmon coupled emission by Au nanobipyramids and its modulation effect on multi-wavelength radiation, Anal. Chim. Acta. 1271 (2023), 341460, https://doi.org/10.1016/j.aca.2023.341460.

[43] S.V. Boriskina, T.A. Cooper, L. Zeng, G. Ni, J.K. Tong, Y. Tsurimaki, Y. Huang, L. Meroueh, G. Mahan, G. Chen, Losses in plasmonics: from mitigating energy dissipation to embracing loss-enabled functionalities, Adv. Opt. Photon. 9 (2017) 775, https://doi.org/10.1364/AOP.9.000775.

[44] W.-S. Chang, B. Willingham, L.S. Slaughter, S. Dominguez-Medina, P. Swanglap, S. Link, Radiative and Nonradiative Properties of Single Plasmonic Nanoparticles and Their Assemblies, Acc. Chem. Res. 45 (2012) 1936–1945, https://doi.org/10.1021/ar200337u.

[45] J. Barthes, A. Bouhelier, A. Dereux, G.C.D. Francs, Coupling of a dipolar emitter into one-dimensional surface plasmon, Sci Rep. 3 (2013) 2734, https://doi.org/10.1038/srep02734.

[46] S. Bhaskar, S.M. Lis S, S. Kanvah, S. Bhaktha, S.S. Ramamurthy, Single-molecule cholesterol sensing by integrating silver nanowire propagating plasmons and graphene oxide π-plasmons on a photonic crystal-coupled emission platform, ACS Appl Opt. Mater. 1 (2023) 159–172, https://doi.org/10.1021/acsaom.2c00026.

[47] S. Bhaskar, A.K. Singh, P. Das, P. Jana, S. Kanvah, S. Bhaktha, S.S. Ramamurthy, Superior resonant nanocavities engineering on the photonic crystal-coupled emission platform for the detection of femtomolar iodide and zeptomolar cortisol, ACS Appl. Mater. Interfaces. 12 (2020) 34323–34336, https://doi.org/10.1021/acsami.0c07515.

[48] K.A. Kang, J. Wang, J.B. Jasinski, S. Achilefu, Fluorescence manipulation by gold nanoparticles: from complete quenching to extensive enhancement, J. Nanobiotechnol. 9 (2011) 16, https://doi.org/10.1186/1477-3155-9-16.

[49] S.-H. Cao, W.-P. Cai, Q. Liu, Y.-Q. Li, Surface plasmon-coupled emission: what can directional fluorescence bring to the analytical sciences? Ann. Rev. Anal. Chem. 5 (2012) 317–336, https://doi.org/10.1146/annurev-anchem-062011-143208.

[50] S. Bhaskar, D. Thacharakkal, S.S. Ramamurthy, C. Subramaniam, Metal-dielectric interfacial engineering with mesoporous nano-carbon florets for 1000-fold fluorescence enhancements: smartphone-enabled visual detection of perindopril erbumine at a single-molecular level, ACS Sustainable Chem. Eng. 11 (2023) 78–91, https://doi.org/10.1021/acssuschemeng.2c04064.

[51] Gaussian 16, Rev. C.01, M. J. Frisch, G. W. Trucks, H. B. Schlegel, G. E. Scuseria, M. A. Robb, J. R. Cheeseman, G. Scalmani, V. Barone, G. A. Petersson, H. Nakatsuji, X. Li, M. Caricato, A. V. Marenich, J. Bloino, B. G. Janesko, R. Gomperts, B. Mennucci, H. P. Hratchian, J. V. Ortiz, A. F. Izmaylov, J. L. Sonnenberg, Williams, F. Ding, F. Lipparini, F. Egidi, J. Goings, B. Peng, A. Petrone, T. Henderson, D. Ranasinghe, V. G. Zakrzewski, J. Gao, N. Rega, G. Zheng, W. Liang, M. Hada, M. Ehara, K. Toyota, R. Fukuda, J. Hasegawa, M. Ishida, T. Nakajima, Y. Honda, O. Kitao, H. Nakai, T. Vreven, K. Throssell, J. A. Montgomery Jr., J. E. Peralta, F. Ogliaro, M. J. Bearpark, J. J. Heyd, E. N. Brothers, K. N. Kudin, V. N. Staroverov, T. A. Keith, R. Kobayashi, J. Normand, K. Raghavachari, A. P. Rendell, J. C. Burant, S. S. Iyengar, J. Tomasi, M. Cossi, J. M. Millam, M. Klene, C. Adamo, R. Cammi, J. W. Ochterski, R. L. Martin, K. Morokuma, O. Farkas, J. B. Foresman, D. J. Fox, Wallingford, CT, **2016**.

[52] R.F.W. Bader, Atoms in Molecules-A Quantum Theory, Oxford University Press, Oxford, 1990.

[53] I.S. Bushmarinov, K.A. Lyssenko, M.Y. Antipin, Atomic energy in the "Atoms in Molecules" theory and its use for solving chemical problems, Russ. Chem. Rev. 78 (2009) 283–302, https://doi.org/10.1070/RC2009v078n04ABEH004017.

[54] C. Lee, W. Yang, R.G. Parr, Development of the Colle-Salvetti correlation-energy formula into a functional of the electron density, Phys. Rev. B. 37 (1988) 785–789, https://doi.org/10.1103/PhysRevB.37.785.

[55] P.J. Stephens, F.J. Devlin, C.F. Chabalowski, M.J. Frisch, Ab initio calculation of vibrational absorption and circular dichroism spectra using density functional force fields, J. Phys. Chem. 98 (1994) 11623–11627, https://doi.org/10.1021/j100096a001.

[56] P.C. Hariharan, J.A. Pople, The influence of polarization functions on molecular orbital hydrogenation energies, Theoret. Chim. Acta. 28 (1973) 213–222, https://doi.org/10.1007/BF00533485.

[57] S. Grimme, J. Antony, S. Ehrlich, H. Krieg, A consistent and accurate ab initio parametrization of density functional dispersion correction (DFT-D) for the 94 elements H-Pu, J. Chem. Phy. 132 (2010), 154104, https://doi.org/10.1063/1.3382344.

[58] F. Neese, F. Wennmohs, U. Becker, C. Riplinger, The ORCA quantum chemistry program package, J. Chem. Phy. 152 (2020), 224108, https://doi.org/10.1063/5.0004608.

[59] J.P. Perdew, Density-functional approximation for the correlation energy of the inhomogeneous electron gas, Phys. Rev. B. 33 (1986) 8822–8824, https://doi.org/10.1103/PhysRevB.33.8822.

[60] Y. Takano, K.N. Houk, Benchmarking the conductor-like polarizable continuum model (CPCM) for aqueous solvation free energies of neutral and ionic organic molecules, J. Chem. Theory Comput. 1 (2005) 70–77, https://doi.org/10.1021/ct049977a.

[61] Q. Zaman, J. Souza, O. Pandoli, K.Q. Costa, V. Dmitriev, D. Fulvio, M. Cremona, R. Q. Aucelio, G. Fontes, T. Del Rosso, Two-color surface plasmon resonance nanosizer for gold nanoparticles, Opt. Express. 27 (2019) 3200, https://doi.org/10.1364/OE.27.003200.

[62] J. Costa, Q. Zaman, K.Q. Da Costa, V. Dmitriev, O. Pandoli, G. Fontes, T. Del Rosso, Limits of the effective medium theory in particle amplified surface plasmon resonance spectroscopy biosensors, Sensors. 19 (2019) 584, https://doi.org/10.3390/s19030584.

[63] S. Bhaskar, N.C.S.S. Kowshik, S.P. Chandran, S.S. Ramamurthy, Femtomolar detection of spermidine using Au decorated SiO 2 nanohybrid on plasmon-coupled extended cavity nanointerface: a smartphone-based fluorescence dequenching approach, Langmuir. 36 (2020) 2865–2876, https://doi.org/10.1021/acs.langmuir.9b03869.

[64] A. Rai, S. Bhaskar, N. Reddy, S.S. Ramamurthy, Cellphone-aided attomolar zinc ion detection using silkworm protein-based nanointerface engineering in a plasmon-coupled dequenched emission platform, ACS Sustainable Chem. Eng. 9 (2021) 14959–14974, https://doi.org/10.1021/acssuschemeng.1c05437.

[65] N. Kongsuwan, A. Demetriadou, R. Chikkaraddy, F. Benz, V.A. Turek, U.F. Keyser, J.J. Baumberg, O. Hess, Suppressed quenching and strong-coupling of purcell-enhanced single-molecule emission in plasmonic nanocavities, ACS Photonics. 5 (2018) 186–191, https://doi.org/10.1021/acsphotonics.7b00668.

[66] K.-X. Xie, L.-T. Xu, Y.-Y. Zhai, Z.-C. Wang, M. Chen, X.-H. Pan, S.-H. Cao, Y.-Q. Li, The synergistic enhancement of silver nanocubes and graphene oxide on surface plasmon-coupled emission, Talanta. 195 (2019) 752–756, https://doi.org/10.1016/j.talanta.2018.11.112.

[67] M.K. Jha, B. Babu, B.J. Parker, V. Surendran, N.R. Cameron, M.M. Shaijumon, C. Subramaniam, Hierarchically engineered nanocarbon florets as bifunctional electrode materials for adsorptive and intercalative energy storage, ACS Appl. Mater. Interfaces. 12 (2020) 42669–42677, https://doi.org/10.1021/acsami.0c09021.

[68] P. Nandi, C. Subramaniam, Employing Redox-Active Additives for Enhanced Charge Polarization and Twofold Higher Energy Density in Supercapacitor, Adv Materials Inter. 10 (2023) 2202052, https://doi.org/10.1002/admi.202202052.

[69] I. Dwivedi, C. Subramaniam, Joule heating-driven transformation of hard-carbons to onion-like carbon monoliths for efficient capture of volatile organic compounds, ACS Mater. Au. 2 (2022) 154–162, https://doi.org/10.1021/acsmaterialsau.1c00062.

[70] J. Saha, R. Ball, C. Subramaniam, Premagnetized carbon-catalyst interface delivering 650% enhancement in electrocatalytic kinetics of hydrogen evolution reaction, ACS Sustainable Chem. Eng. 9 (2021) 7792–7802, https://doi.org/10.1021/acssuschemeng.1c01095.

[71] M. Moronshing, A. Sah, V. Kalyani, C. Subramaniam, Nanostructured carbon florets as scavenger of As 3+, Cr 6+, Cd 2+, and Hg 2+ for water remediation, ACS Appl. Nano Mater. 3 (2020) 468–478, https://doi.org/10.1021/acsanm.9b02052.

[72] A.M. Siddiq, R. Thangam, B. Madhan, M.S. Alam, Counterion coupled (COCO) gemini surfactant capped Ag/Au alloy and core-shell nanoparticles for cancer therapy, RSC Adv. 9 (2019) 37830–37845, https://doi.org/10.1039/C9RA06494J.

[73] M. Murugavelu, B. Karthikeyan, Synthesis, characterization of Ag-Au core-shell bimetal nanoparticles and its application for electrocatalytic oxidation/sensing of l-methionine, Mater. Sci. Eng. c. 70 (2017) 656–664, https://doi.org/10.1016/j.msec.2016.09.046.

[74] C. Krishnaraj, V.K. Kaliannagounder, R. Rajan, T. Ramesh, C.S. Kim, C.H. Park, B. Liu, S.-I. Yun, Silver nanoparticles decorated reduced graphene oxide: Eco-friendly synthesis, characterization, biological activities and embryo toxicity studies, Environ. Res. 210 (2022), 112864, https://doi.org/10.1016/j.envres.2022.112864.

[75] A. Sah, S. Sharma, S. Saha, C. Subramaniam, Phonon-engineered hard-carbon nanoflorets achieving rapid and efficient solar-thermal based water evaporation and space-heating, ACS Appl. Mater. Interfaces 15 (37) (2023) 43810–43821, https://doi.org/10.1021/acsami.3c09078.

[76] A. Sah, A.K. Mandal, S. Tiwari, S. Mukherji, C. Subramaniam, Scalable and high throughput photothermal water disinfection with negligible CO2 footprint utilizing nanostructured carbon coatings, Npj Clean Water 6 (2023) 75, https://doi.org/10.1038/s41545-023-00284-4.

[77] S. Bhaskar, P. Das, M. Moronshing, A. Rai, C. Subramaniam, S.B.N. Bhaktha, S. S. Ramamurthy, Photoplasmonic assembly of dielectric-metal, Nd 2 O 3 -Gold soret nanointerfaces for dequenching the luminophore emission, Nanophotonics. 10 (2021) 3417–3431, https://doi.org/10.1515/nanoph-2021-0124.

[78] S. Bhaskar, R. Patra, N.C.S.S. Kowshik, K.M. Ganesh, V. Srinivasan, P. Chandran, S. S. Ramamurthy, Nanostructure effect on quenching and dequenching of quantum emitters on surface plasmon-coupled interface: A comparative analysis using gold nanospheres and nanostars, Phys. e: Low-Dimens. Syst. Nanostruct. 124 (2020), 114276, https://doi.org/10.1016/j.physe.2020.114276.

[79] A. Rai, S. Bhaskar, K.M. Ganesh, S.S. Ramamurthy, Gelucire®-mediated heterometallic AgAu nanohybrid engineering for femtomolar cysteine detection using smartphone-based plasmonics technology, Mater. Chem. Phys. 279 (2022), 125747, https://doi.org/10.1016/j.matchemphys.2022.125747.

[80] S. Bhaskar, P. Jha, C. Subramaniam, S.S. Ramamurthy, Multifunctional hybrid soret nanoarchitectures for mobile phone-based picomolar Cu2+ ion sensing and dye degradation applications, Phys. e: Low-Dimens. Syst. Nanostruct. 132 (2021), 114764, https://doi.org/10.1016/j.physe.2021.114764.

[81] S. Bhaskar, S.S. Ramamurthy, Synergistic coupling of titanium carbonitride nanocubes and graphene oxide for 800-fold fluorescence enhancements on smartphone based surface plasmon-coupled emission platform, Mater. Lett. 298 (2021), 130008, https://doi.org/10.1016/j.matlet.2021.130008.

[82] S. Bhaskar, V. Srinivasan, S.S. Ramamurthy, Nd 2 O 3 -Ag Nanostructures for Plasmonic Biosensing, Antimicrobial, and Anticancer Applications, ACS Appl. Nano Mater. 6 (2023) 1129–1145, https://doi.org/10.1021/acsanm.2c04643.

[83] P. Zhou, Why the lowest electronic excitations of rhodamines are overestimated by time-dependent density functional theory, Int. J. Quantum Chem. 118 (2018) e25780.

[84] R.F. Menger, J.J. Beck, T. Borch, C.S. Henry, 2, ACS EST, Water. 2 (2022) 565–572, https://doi.org/10.1021/acsestwater.1c00356.

[85] L.D. Chen, C.-Z. Lai, L.P. Granda, M.A. Fierke, D. Mandal, A. Stein, J.A. Gladysz, P. Bühlmann, 9, Anal. Chem. 85 (2013) 7471–7477, https://doi.org/10.1021/ac401424j.

[86] J. Gong, T. Fang, D. Peng, A. Li, L. Zhang, A highly sensitive photoelectrochemical detection of perfluorooctanic acid with molecularly imprinted polymer-functionalized nanoarchitectured hybrid of AgI–BiOI composite, Biosens. Bioelectron. 73 (2015) 256–263, https://doi.org/10.1016/j.bios.2015.06.008.

[87] J. Liu, J. Du, Y. Su, H. Zhao, 7, Microchem. J. 149 (2019), 104019, https://doi.org/10.1016/j.microc.2019.104019.

[88] Z. Cheng, F. Zhang, X. Chen, L. Du, C. Gao, K. Tan, Highly sensitive and selective detection of perfluorooctane sulfonate based on the Janus Green B resonance light scattering method, Anal. Methods. 8 (2016) 8042–8048, https://doi.org/10.1039/C6AY02739C.

[89] T. Tran, T, J. Li, H. Feng, J. Cai, L. Yuan, N. Wang, Q. Cai, 1, Sensors and Actuators B: Chemical. 190 (2014) 745–751. https://doi.org/10.1016/j.snb.2013.09.048.

[90] R. Ranaweera, C. Ghafari, L. Luo, Bubble-nucleation-based method for the selective and sensitive electrochemical detection of surfactants, Anal. Chem. 91 (2019) 7744–7748, https://doi.org/10.1021/acs.analchem.9b01060.

[91] N. Karimian, A.M. Stortini, L.M. Moretto, C. Costantino, S. Bogialli, P. Ugo, Electrochemosensor for trace analysis of perfluorooctanesulfonate in water based on a molecularly imprinted poly(o -phenylenediamine) polymer, ACS Sens. 3 (2018) 1291–1298, https://doi.org/10.1021/acssensors.8b00154.